Quantifying Uncertainty in Ice Particle Velocity–Dimension Relationships Using MC3E Observations

ANDREW M. DZAMBO,[a] GREG MCFARQUHAR,[a,b] AND JOSEPH A. FINLON[c]

[a] *Cooperative Institute for Severe and High Impact Weather and Research Operations, University of Oklahoma, Norman, Oklahoma*
[b] *School of Meteorology, University of Oklahoma, Norman, Oklahoma*
[c] *Department of Atmospheric Sciences, University of Washington, Seattle, Washington*

(Manuscript received 10 December 2021, in final form 4 August 2022)

ABSTRACT: Ice particle terminal fall velocity (V_t) is fundamental for determining microphysical processes, yet remains extremely challenging to measure. Current theoretical best estimates of V_t are functions of Reynolds number. The Reynolds number is related to the Best number, which is a function of ice particle mass, area ratio (A_r), and maximum dimension ($D_{\max}$). These estimates are not conducive for use in most models since model parameterizations often take the form $V_t = \alpha D_{\max}^{\beta}$, where ($\alpha$, β) depend on habit and $D_{\max}$. A previously developed framework is used to determine surfaces of equally plausible (α, β) coefficients whereby ice particle size/shape distributions are combined with V_t best estimates to determine mass- (V_M) or reflectivity-weighted (V_Z) velocities that closely match parameterized $V_{M,\mathrm{SD}}$ or $V_{Z,\mathrm{SD}}$ calculated using the (α, β) coefficients using two approaches. The first uses surfaces of equally plausible (a, b) coefficients describing mass (M)–dimension relationships (i.e., $M = \alpha D_{\max}^{b}$) to calculate mass- or reflectivity-weighted velocity from size/shape distributions that are then used to determine (α, β) coefficients. The second investigates how uncertainties in A_r, $D_{\max}$, and size distribution $N(D)$ affect V_M or V_Z. For seven of nine flight legs flown on 20 and 23 May 2011 during the Mesoscale Continental Convective Clouds Experiment (MC3E), uncertainty from natural parameter variability—namely, the variability in ice particle parameters in similar meteorological conditions—exceeds uncertainties arising from different A_r assumptions or $D_{\max}$ estimates. The combined uncertainty between A_r, $D_{\max}$, and $N(D)$ produced smaller variability in (α, β) compared to varying $M(D)$, demonstrating $M(D)$ must be accurately quantified for model fall velocities. Primary sources of uncertainty vary considerably depending on environmental conditions.

SIGNIFICANCE STATEMENT: Ice particle fall velocity is fundamental for numerous processes within clouds, and hence is a critical property that must be accurately represented in weather and climate models. Using aircraft observations of ice particle shapes and sizes obtained in clouds behind midlatitude thunderstorms, this work develops a new framework for estimating ice particle fall velocities and their uncertainty, including quantifying the importance of different uncertainty sources from cloud microphysics measurements. Natural parameter variability contributes the most uncertainty in ice particle fall velocity estimates, although other sources can also be important contributors to uncertainty in certain conditions. Additional work examining ice particle data is needed to further understand how dependent uncertainty in certain ice particle properties are to local environmental conditions.

KEYWORDS: Clouds; Cloud microphysics; Ice crystals; Ice particles; Cloud parameterizations; Aircraft observations

1. Introduction

One of the most fundamental properties of ice crystals relevant for understanding cloud microphysical processes is terminal fall velocity (referred to as fall velocity hereafter; see AMS Glossary of Meteorology). An ice crystal's shape, maximum dimension perpendicular to the direction of its fall, and density are most important in determining its fall velocity (e.g., Locatelli and Hobbs 1974; Mitchell et al. 1990). Ice particle fall velocity represents a key facet for numerous important processes in the atmosphere such as water vapor redistribution (Bony et al. 2008; D'Alessandro et al. 2019), changes to vertical latent and radiative heating profiles (Nelson and L'Ecuyer 2018), microphysical evolution of precipitation including hail formation, aggregation, riming, and sublimation (Heymsfield et al. 1980; McFarquhar et al. 2006; A. J. Jensen et al. 2017; Stanford et al. 2017; Chase et al. 2018; Bühl et al. 2019; Finlon et al. 2020; Morrison et al. 2020; Huang et al. 2021; Tobin and Kumjian 2021; Shates et al. 2021), surface energy and hydrologic balance (Daloz et al. 2018), and feedbacks within weather and climate models (Bony et al. 2015; Hofer et al. 2019; Wang et al. 2020; Sledd and L'Ecuyer 2021). Quantifying fall velocities and their uncertainties is also critical for accurate cloud and precipitation remote sensing retrievals (e.g., Matrosov and Heymsfield 2000; Barrett et al. 2019; Chase et al. 2021). Finally, ice crystal fall velocity is one of the most important parameters determining climate sensitivity (Sanderson et al. 2008) through its impact on ice cloud coverage (Klein and Jakob 1999; Mitchell et al. 2008).

Dating back to the earliest known studies on ice crystal fall velocities (Nakaya and Terada 1935; Heymsfield 1972, and references therein), ice particle fall velocities and their uncertainties have been notoriously difficult to quantify for many reasons. An ice particle's fall velocity depends on its mass, density, shape (or habit), and dimension (Locatelli and Hobbs 1974;

Corresponding author: Andrew Dzambo, dzamboam@ou.edu

DOI: 10.1175/JAS-D-21-0322.1

Heymsfield et al. 2002, 2004; Schmitt and Heymsfield 2010; Mascio et al. 2017; Magee et al. 2021; Bailey and Hallett 2009), all of which are very difficult to directly measure in real time. Varying environmental conditions (temperature, pressure, humidity), convective properties and large-scale synoptic conditions largely dictate ice particle properties (Dzambo and Turner 2016; Hu et al. 2021). In addition to environmental variability, ice crystals are typically not observed in the conditions where they grew and instrument limitations add uncertainty to fall velocity estimates (Brandes et al. 2008; Finlon et al. 2019). Regardless of environmental conditions, ice particle fall velocities fluctuate during descent (Nettesheim and Wang 2018), adding a small but potentially important source of uncertainty.

Following earlier studies by List and Schemenauer (1971), Locatelli and Hobbs (1974), Böhm (1989), and others, Mitchell (1996, denoted MI96 hereafter) developed a method for computing ice particle fall velocity from particle mass and projected area. This method predicted ice crystal fall velocity to within 20% of reference laboratory measurements. Several other studies that developed fall velocity relationships based upon ice particle maximum dimension, mass, or projected area (e.g., Erfani and Mitchell 2017; Vázquez-Martín et al. 2021a,b) noted a variety of uncertainties and error estimates associated with fall velocity computations. For example, Heymsfield and Westbrook (2010, denoted HW10 hereafter) addressed an issue where ice particles with low area ratios (i.e., the ratio of the projected area of the ice crystal to the smallest possible circle that would enclose the ice crystal; see McFarquhar and Heymsfield 1996) contributed large uncertainties to computed fall velocities. Schmitt et al. (2019) computed statistical probabilities of terminal velocity for ice particles of the same size and found that variability increases by at least 20% with increasing temperature and particle size.

Ice particle fall velocities have been overly simplified in weather and climate models (Baumgardner et al. 2012), with many studies referenced hereafter citing ice particle fall velocities as a key source of uncertainty in their results and/or a critical area of investigation for future modeling- or observation-based studies. Recent improvements to the representation of ice particles in the Predicted Particle Properties (P3) scheme (Morrison and Milbrandt 2015) have balanced increased complexity without sacrificing computational efficiency (e.g., Milbrandt et al. 2021). In the P3 scheme and all other bulk microphysics schemes, ice sedimentation fluxes are computed via moment-weighted (e.g., mass or reflectivity) fall speeds. These moment-weighted fall speeds directly impact microphysical process rates (e.g., McFarquhar and Black 2004) and all prognostic ice variables including total ice mass, rime ice mass, total ice number, and rime ice volume in the P3 scheme (Milbrandt et al. 2021). Milbrandt et al. (2021) showed that such treatments in a triple-moment version of P3 improved the representation of hail. Xue et al. (2017), motivated by the idea that bin microphysics schemes should be more accurate and realistic compared to bulk microphysics schemes, found that both microphysics schemes produce qualitatively similar results when creating idealized simulations of a squall line and concluded that improved representation of ice particle velocities (among other properties) and their uncertainty is necessary to isolate the impact of physics on weather system evolution. Stanford et al. (2019) showed how variations in velocity–dimension relationships resulted in varying rainfall rates and total accumulated rainfall for selected Mesoscale Continental Convective Clouds Experiment (MC3E; Jensen et al. 2015, 2016) case studies. These recent studies demonstrate a need to understand variations in ice particle fall velocities and to reduce uncertainty in ice particle fall velocity representations.

While direct airborne measurements of ice particle fall velocities are not currently made, numerous prior studies have advanced the ability to estimate fall velocities from airborne measurements. Over the past three decades, ice particle datasets have been cataloged from numerous airborne field campaigns representing a variety of environmental conditions (e.g., McFarquhar and Heymsfield 1996; McFarquhar et al. 2007; Jensen et al. 2013; Spichtinger and Krämer 2013; Jensen et al. 2016; Krämer et al. 2016; E. J. Jensen et al. 2017). In addition to the wide variety of environmental conditions sampled through such campaigns, advances in the interpretation of airborne ice particle measurements such as accounting for ice particle shattering (Korolev et al. 2011; Jackson et al. 2014) and instrument mounting location (Afchine et al. 2018) have improved confidence in analyses resulting from these datasets.

Given that multiple sources of uncertainty contribute to variations in derived ice particle parameters, McFarquhar et al. (2015) developed a framework to represent parameters (i.e., gamma fit parameters) describing ice particle size distributions (PSDs hereafter) as volumes of equally plausible solutions in the phase space of the parameters rather than as fixed values. They also showed that the parameters used to quantify particle size distributions are codependent to a high degree. McFarquhar et al. (2015) also showed that, for a fixed mass–dimensional relationship, terminal velocity varied by 0.15 m s^{-1} for equally plausible parameters describing a number distribution function $N(D)$. Using airborne data from MC3E, Finlon et al. (2019) expanded this framework to compute equally plausible mass–dimension relationship parameters for varying environmental conditions and elucidated the relative roles of size distribution uncertainties relative to measurement uncertainty and the natural variability of the parameters. Natural variability in this context implies that (α, β) have varying values due to differences in $N(D)$, A_r, and other parameters even in the same environmental conditions. Ding et al. (2020) similarly expanded this framework to quantify the role of ice particle maximum dimension uncertainty on resulting mass–dimension relationship parameters.

This present study builds upon these frameworks by contextualizing how equally plausible mass–dimension relationships affect resulting mean fall velocity estimates, while also evaluating how measurement uncertainties in size distributions, area ratios and maximum dimension as well as the natural variability of parameters contribute to the spread in fall velocity estimates. Although this study does not involve any direct modeling work demonstrating how uncertainty in ice particle fall velocity affects model simulations, it does provide a foundation whereby uncertainties in ice particle fall velocities can be tested in the P3 and related microphysics schemes.

The remainder of the paper is organized as follows. Section 2 describes the MC3E campaign and those measurements from the MC3E campaign used in this study. Section 3 describes the quantification of fall velocity and fall velocity uncertainties, and the development of a framework for determining surfaces of equally plausible fall velocities applicable to modeling studies. Sections 4 and 5 discuss results from two methods testing the aforementioned framework, and conclusions are presented in section 6. The two methods described in this work aim to address the following science questions:

1) If a number of equally plausible mass–dimension (M–D hereafter) relationships can describe a population of ice particles, how much variability arises among velocity–dimension (V–D hereafter) parameters when accounting for all plausible M–D relationships?
2) What are the key sources of uncertainty determining the variability of the equally plausible V–D relationships, and how do these compare to those for the uncertainty arising from varying but equally plausible M–D relationships?

2. Datasets

A brief overview of the MC3E campaign is presented here, as well as the data and procedures used to compute ice particle fall velocities and their uncertainties. The list of abbreviations used throughout this study are given in the appendix.

a. MC3E campaign

The MC3E field campaign, led jointly by the U.S. National Aeronautics and Space Administration (NASA) Global Precipitation Measurement (GPM) and Department of Energy's (DOE) Atmospheric Radiation Measurement (ARM) programs, took place from 22 April 2011 through 6 June 2011 over the Southern Great Plains (SGP) centered on south-central Oklahoma (Jensen et al. 2016). Instruments aboard the University of North Dakota's Citation aircraft and synergistic suite of ground-based radars, radiosondes, and disdrometers were used to generate a comprehensive dataset aimed at improving the understanding of processes leading to convection initiation, the dynamical evolution of deep convection, and the microphysical evolution of rainfall, hail, and ice within observed mesoscale convection. Two flights highlighted in this study from 20 and 23 May 2011 sampled a mesoscale convective system (MCS) and a supercell thunderstorm, respectively. The analysis presented here focuses on observations collected during constant altitude (at near-constant temperature) flight legs where only ice phase hydrometeors were observed and where coincident radar reflectivity measurements exist. Choosing near-constant temperature flight legs also allows for the assumption that all measured ice particles along a given flight leg are representative of the same particle growth environment. Coincident radar reflectivity data from the Vance Air Force Base (location: 36.3393°N, 97.9131°W) WSR-88D (S band) are collocated to coincident aircraft measurements using the Python ARM Radar Toolkit (PyART; Helmus and Collis 2016) and the Airborne Weather Observation Toolkit radar matching algorithm (Nesbitt et al. 2019). Finally, for consistency, radar reflectivity measurements are quality controlled following section 5.1 in Finlon et al. (2019).

b. OAP datasets

Data from two Optical Array Probes (OAPs), namely, a Two-Dimensional Cloud Probe (2D-C) and the High Volume Precipitation Spectrometer (HVPS), were used. Data from both probes were processed using the University of Illinois/Oklahoma OAP Processing Software (UIOOPS; McFarquhar et al. 2018). The 2D-C and HVPS each record two-dimensional images of ice particles with size resolutions of 30- and 150-μm resolution, respectively. Composite particle size distributions (PSDs) were generated using 1-s averaged 2D-C and HVPS PSDs as a function of particle maximum dimension D defined following Wu and McFarquhar (2016), using a 1 mm cutoff between the probes following Finlon et al. (2019). Particles with $D < 150$ μm were excluded due to large uncertainties in the derived number distribution function $N(D)$ because of a small and poorly defined sample volume, the small numbers of photodiodes shadowed, and potential impact of shattered particles (Baumgardner and Korolev 1997; McFarquhar et al. 2017, and references therein). Within UIOOPS, best estimates of ice particle mass were computed using a number of different techniques. Ice particle habits are first identified using modifications to the Holroyd (1987) methodology (Jackson et al. 2014). Appropriate coefficients for mass $M(D)$ and area $A(D)$ relationships for each habit class are then determined, where $m(D) = aD^b$ and $A(D) = \nu D^\sigma$. Of importance for this work is the ice particle area ratio (A_r), which is determined using this best-estimate $A(D)$ for the identified habit and then computed as $A_r = A(D)/[(\pi/4)D^2]$ for use in the fall velocity calculations (see section 3). Table 1 lists the $M(D)$ and $A(D)$ relationships corresponding to the habit classification used in this study. Though not considered in this study, a second option for computing mass follows the Baker and Lawson (2006) approach using direct measurements of projected area derived from the crystal images and $D_{\max}$ to estimate mass. For ice particles with a best estimate mass and known area ratio, a terminal velocity can be computed following the method outlined in section 3.

3. Fall velocity computations and uncertainty estimates

Many field and laboratory experiments measuring ice particle fall velocities have been used as a basis for finding the best power-law representation for fall speed (V) as a function of D (e.g., Kajikawa 1973; Locatelli and Hobbs 1974; Khvorostyanov and Curry 2002, 2005) for use in weather and climate models following

$$V(D) = \alpha D^\beta, \tag{1}$$

where α is a prefactor (often in units of $m^{1-\beta}$ s^{-1}) and β is an exponent. The α and β are typically derived by determining the values that provide the best characterization of V as a function of D. Both α and β are also adjusted to sea level pressure (SLP; taken to be 1000 mb in this study) and any reference of $V(D)$ hereafter implies α and β are representative of SLP conditions.

TABLE 1. A summary of mass–dimension $M(D)$ and area–dimension $A(D)$ habit-dependent parameters used to generate the best-estimate V_T dataset. Note that a "tiny" particle is defined as a 2D-C or an HVPS particle image containing 25 or fewer pixels. Each $M(D)$ and $A(D)$ relationship is listed in Table 1 of MI96 except for those under the "spherical" or "tiny" classification, which are defined based on Brown and Francis (1995).

Habit classification	$M(D) = aD^b$ (g)	$A(D) = aD^b$ (mm^2)
Spherical	$a = 0.002\,940$, $b = 1.90$	$a = 0.2285$, $b = 1.88$
Linear	$a = 0.000\,907$, $b = 1.74$	$a = 0.0696$, $b = 1.50$
Oriented	$a = 0.000\,907$, $b = 1.74$	$a = 0.0696$, $b = 1.50$
Tiny	$a = 0.002\,940$, $b = 1.90$	$a = 0.2285$, $b = 1.88$
Hexagonal	$a = 0.007\,390$, $b = 2.45$	$a = 0.6500$, $b = 2.00$
Irregular	$a = 0.002\,940$, $b = 1.90$	$a = 0.2285$, $b = 1.88$
Graupel	$a = 0.049\,000$, $b = 2.80$	$a = 0.5000$, $b = 2.00$
Dendrite	$a = 0.000\,516$, $b = 1.80$	$a = 0.2100$, $b = 1.76$
Aggregate	$a = 0.002\,940$, $b = 1.90$	$a = 0.2285$, $b = 1.88$

A well-known caveat to using V–D relationships is the fact that area ratio, particle dimension, and size distribution measurements introduce uncertainty because each of these properties has their own individual measurement uncertainty. Furthermore, equally plausible M–D relationships accounting for measurement uncertainties and natural variability also lead to uncertainty in V–D relationships. However, the relative magnitude of their uncertainty relative to the aforementioned uncertainties in area ratio, maximum dimension, and size distribution is unknown. The following subsections highlight the procedures used to compute ice particle fall velocity and its uncertainty.

a. Fall velocity computation

Direct measurements of ice particle terminal velocities have not been previously obtained with airborne instrumentation. The most reliable measurements of ice crystal terminal velocities have been obtained in laboratory experiments and ground-based studies or field campaigns (e.g., Kajikawa 1973; Locatelli and Hobbs 1974; MI96; HW10). The terminal velocity of an ice crystal is computed as

$$V_T(D) = \frac{\eta R_e}{\rho_a D}, \tag{2}$$

where R_e is the Reynolds number, η the dynamic viscosity of air (kg m^{-1} s^{-1}), ρ_a the density of air, and D is determined from 2D-C and HVPS data. The air density ρ_a is pressure dependent, implying V_T is also a function of air pressure. Following Heymsfield (1972), V_T is adjusted to SLP following

$$V_{T,1000} = V_T \times \left(\frac{P}{P_{1000}}\right)^{0.5}, \tag{3}$$

where P is the air pressure of the aircraft and P_{1000} is the sea level pressure. The Reynolds number (e.g., Beard 1980; Böhm 1989) can be expressed as

$$R_e = \frac{\delta_0^2}{4}\left(\left\{1 + \frac{4X[m(D)]}{\delta_0^2\sqrt{C_0}}\right\}^{1/2} - 1\right)^2, \tag{4}$$

where the Best or Davies number X (Davies 1945; Best 1950) is a dimensionless quantity that represents the drag of a falling sphere into a fluid. The Best number can be formulated as (e.g., Beard 1980; Khvorostyanov and Curry 2005)

$$X[m(D)] = \frac{8\rho_a g}{\pi\eta^2 A_r}\, m(D) \tag{5}$$

or, using the HW10 approach for a "modified" Best number X^*, as

$$X^*[m(D)] = \frac{8\rho_a g}{\pi\eta^2 A_r^k}\, m(D), \tag{6}$$

where A_r represents the ice crystal area ratio. The exponential k in Eq. (6) represents a correction factor to the area ratio and is set to 0.5 following HW10. Finally, g is gravity, C_0 is a drag coefficient approximated as 0.6, and δ_0 is a dimensionless coefficient set to 5.83 when using Eq. (5) (Böhm 1989), or C_0 is set to 0.35 and δ_0 is set to 8 when using Eq. (6) (HW10). The value of V_T is computed using Eqs. (2)–(6) for every ice particle observed by the OAPs described in section 2.

Computations of V_T for individual ice particles are not directly applied in modeling applications that use bulk parameterization schemes. For such schemes, the mass-weighted mean fall velocity (V_M) of a population of ice crystals is used to characterize their motion and is written as

$$V_M = \frac{\int_0^\infty V_T(D)m(D)N(D)dD}{\int_0^\infty m(D)N(D)dD}, \tag{7a}$$

or for a number of discrete size bins as

$$V_M = \frac{\sum_{i=1}^{K} V_T(D_i)(m(D_i))N(D_i)\Delta D_i}{\sum_{i=1}^{K}[m(D_i)]N(D_i)\Delta D_i}, \tag{7b}$$

where $N(D)$ $[N(D_i)]$ is the number distribution function of particles with dimension $D(D_i)$. Equation (7a) represents the general form for computing a mass-weighted fall velocity based on a continuous distribution, as generally assumed in bulk schemes. However, since measured ice crystals are sorted

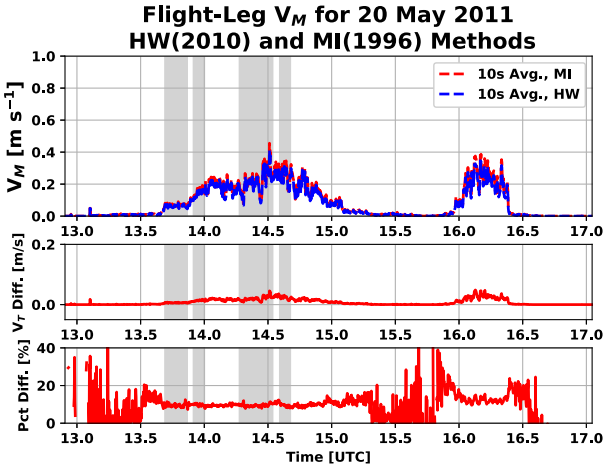

FIG. 1. (top) The 10-s, mass-weighted, mean flight-level fall velocity for the 20 May 2011 research flight using HW10 (blue) and MI96 (red) methods applied to composite 2D-C/HVPS PSD and (middle) the difference in V_M estimates and (bottom) percent difference in V_M estimates. Also shown are the flight segments analyzed in this paper (highlighted in gray) and follow the flight segments analyzed in Finlon et al. (2019) for consistency.

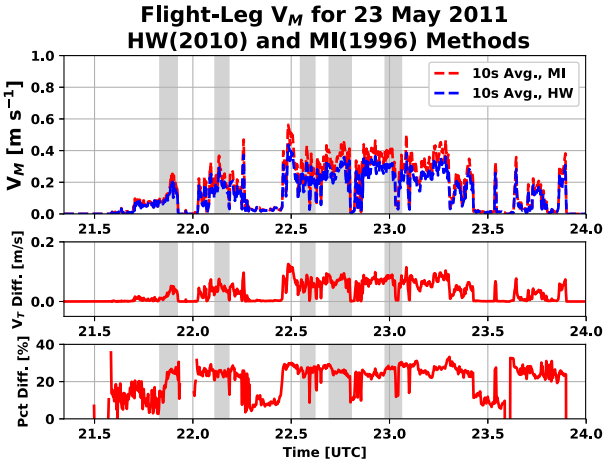

FIG. 2. As in Fig. 1, but for the 23 May 2011 flight.

into size bins of width ΔD_i with midpoint D_i, it is more convenient to use the discrete form of Eq. (7b) for computing V_M. To compare model fields against radar reflectivity observations, a reflectivity-weighted fall velocity (V_Z) is frequently used (e.g., Hogan et al. 2006) and can be expressed as, assuming Rayleigh scattering,

$$V_Z = \frac{\int_0^\infty V_T(D)[m(D)]^2 N(D) dD}{[m(D)]^2 N(D) dD}, \tag{8a}$$

or expressed in discrete form as

$$V_Z = \frac{\sum_{i=1}^{K} V_T(D_i)[m(D_i)]^2 N(D_i) dD}{\sum_{i=1}^{K} [m(D_i)]^2 N(D_i) dD}. \tag{8b}$$

Hereafter, $V_{M,Z}$ represents either V_M or V_Z.

Although direct measurements of A_r are obtained from the 2D-C and HVPS two-dimensional images, there are uncertainties induced by the orientation of the crystals relative to the imaging lasers. Further, direct estimates of A_r are only possible for crystals entirely within the photodiode array. This will be addressed in future work. Even though crystals typically fall with their maximum dimension oriented perpendicular to the fall direction, both McFarquhar et al. (1999) and Um and McFarquhar (2011) showed substantial variability in both D and A_r for the imaging of ice crystal habits and that D derived from UIOOPS is not the true maximum dimension of a three-dimensional ice crystal. This is particularly problematic for ice crystals with low A_r such as dendrites or stellar crystals (HW10). Hence, HW10 improved V_T estimates for low A_r ice crystals through a k-factor correction [i.e., A_r^k in Eq. (6)].

The mean mass- and reflectivity-weighted fall velocities include several sources of uncertainty, which must be accounted for, in order to develop equally realizable solutions of $V_{M,Z}$ as needed in bulk microphysics schemes. The best estimates of $M(D_i)$ are used to compute V_M and V_Z following Eqs. (7b) and (8b). The next two subsections outline the process for computing the effect of varying equally realizable $M(D)$ on V_M and V_Z, as well as uncertainties in V_M and V_Z associated with the ice particle area ratio, maximum dimension, size distribution, and natural variability of microphysical parameters within similar environmental conditions.

Figures 1 and 2 show the 10-s averaged V_M for the 20 and 23 May 2011 flights (respectively) computed using the HW10 and MI96 methods. The difference in terminal velocity between the two methods is at least 0.03 m s^{-1} (0.06 m s^{-1}) for terminal velocities exceeding 0.3 m s^{-1} for the 20 May 2011 (23 May 2011) flight. For all 23 May 2011 flight legs, the percent difference between the V_t estimates is over 20%, which is larger than the 10%–15% difference noted for the 20 May 2011 flight legs. Tiny ice particles (i.e., less than 25 pixels or within the 150–200 μm range if measured by the 2D-C; less than 25 pixels or within the 1–2 mm range if measured by the HVPS) contribute over half of the total sampled mass for the 23 May 2011 flight (see Table 2). Noting that approximately 95% of the total mass for all flight legs was observed by the 2D-C, the higher percent increase in V_t between the HW10 and MI96 computations is consistent with the finding from HW10 that fall velocities were overestimated by the MI96 methods for smaller ice particles. In fact, concentrations of tiny particles between 150 and 200 μm were nearly an order of magnitude higher for all 23 May 2011 flight segments compared to the 20 May 2011 flight segments (Figs. 3 and 4).

b. *Effect of equally plausible M(D) relations on V(D)*

This section describes how the use of equally plausible surfaces of (a, b) coefficients in $M(D)$ relationships affects the spread of (α, β) coefficients in $V(D)$ relationships. To

TABLE 2. Summary of mean flight temperature, altitude, duration, and percent mass of each ice particle habit for flight legs used in this analysis. The mean temperature and altitude data contained in this table were adapted from Table 1 in Finlon et al. (2019).

Flight segment	Mean temp (°C)	Mean altitude (km)	Spherical (%)	Linear (%)	Oriented (%)	Tiny (%)	Hexagonal (%)	Irregular (%)	Graupel (%)	Dendrite (%)	Aggregate (%)
1341:25–1352:00 UTC 20 May 2011	−5.6	5.0	24	4	2	8	56	5	0	1	0
1354:05–1400:05 UTC 20 May 2011	−10.4	5.9	25	4	2	8	55	5	0	1	0
1416:32–1432:15 UTC 20 May 2011	−22.7	7.9	26	3	2	9	54	5	0	1	0
1435:30–1440:35 UTC 20 May 2011	−16.4	6.9	25	3	3	10	53	5	0	1	0
2149:55–2155:15 UTC 23 May 2011	−25.0	7.9	10	3	3	55	27	2	0	0	0
2206:45–2211:00 UTC 23 May 2011	−25.3	7.9	10	3	3	55	27	2	0	0	0
2232:50–2237:15 UTC 23 May 2011	−34.7	9.1	10	3	3	54	28	2	0	0	0
2241:35–2248:20 UTC 23 May 2011	−34.2	9.1	10	3	3	53	29	2	0	0	0
2258:40–2303:40 UTC 23 May 2011	−34.4	9.1	9	3	3	54	29	2	0	0	0

compute the spread of (α, β) coefficients, this study adapts recently developed methodologies by McFarquhar et al. (2015), Finlon et al. (2019), and Ding et al. (2020) using a χ^2 minimization procedure. A χ^2minimization procedure is ideal for investigating uncertainty in ice particle fall velocity uncertainty because it allows for multiple sources of uncertainty to be included *and* allows for each source to be computed and compared independently of one another. To outline the χ^2 minimization procedure, the Finlon et al. (2019) study that determined equally plausible (a, b) parameters in $M(D)$ relationships is briefly described here. Finlon et al. (2019) minimized the χ^2 difference between the total ice water content and radar reflectivity estimated from the size distributions with those measured directly by the Nevzorov probe (Korolev et al. 1998) and by the radar at Vance Air Force Base, using a quantity χ^2_T defined for a given set of (a, b) coefficients as

$$\chi^2_T(a,b) = \frac{1}{N}\sum_{i=1}^{N}[TWC_{\text{diff}}(i) + Z_{\text{diff}}(i)], \tag{9a}$$

where χ^2_T minimizes the summation of TWC_{diff} and Z_{diff} over N 10-s data points for a given flight leg, where TWC_{diff} and Z_{diff} represent metrics describing a weighted difference between the measured TWC and Z and those computed from the observed size distributions (denoted by the subscript SD) such that $\text{TWC}_{\text{diff}} = \{[\text{TWC} - \text{TWC}_{\text{SD}}(a,b)]/\sqrt{\text{TWC} \times \text{TWC}_{\text{SD}}(a,b)}\}^2$ and $Z_{\text{diff}} = \{[\sqrt{Z} - \sqrt{Z_{\text{SD}}(a,b)}]/\sqrt{\sqrt{Z} \times \sqrt{Z_{\text{SD}}(a,b)}}\}^2$, whereby the ($a$, b) that minimize χ^2_T is determined, eliminating the need to assume any $M(D)$ for a given sample volume. The underestimate of TWC measured by the Nevzorov probe in the presence of larger ice crystals has been documented in previous studies (e.g., Faber et al. 2018), and motivates the additional use of reflectivity to create the equally realizable surfaces shown in section 4. For field campaigns where airborne TWC data may not be available or are deemed problematic, or otherwise for applications where only radar reflectivity data are available, χ^2_Z can be used instead where

$$\chi^2_Z(a,b) = \frac{1}{N}\sum_{i=1}^{N}[Z_{\text{diff}}(i)]. \tag{9b}$$

For this study, both the χ^2_T cost function for $M(D)$ from Eq. (6) in Finlon et al. [2019; adapted as Eq. (9a) for this work] and the χ^2_Z cost function using only radar reflectivity [Eq. (9b)] following Ding et al. (2020) are used. A key result from Finlon et al. (2019) is that the range of plausible b computed was significantly larger for flight legs on 20 May 2011 compared to the range for 23 May 2011, likely because of the fact that b increases with increasing temperature and IWC, both of which increased during the 20 May 2011 case. The prefactor a also had much less

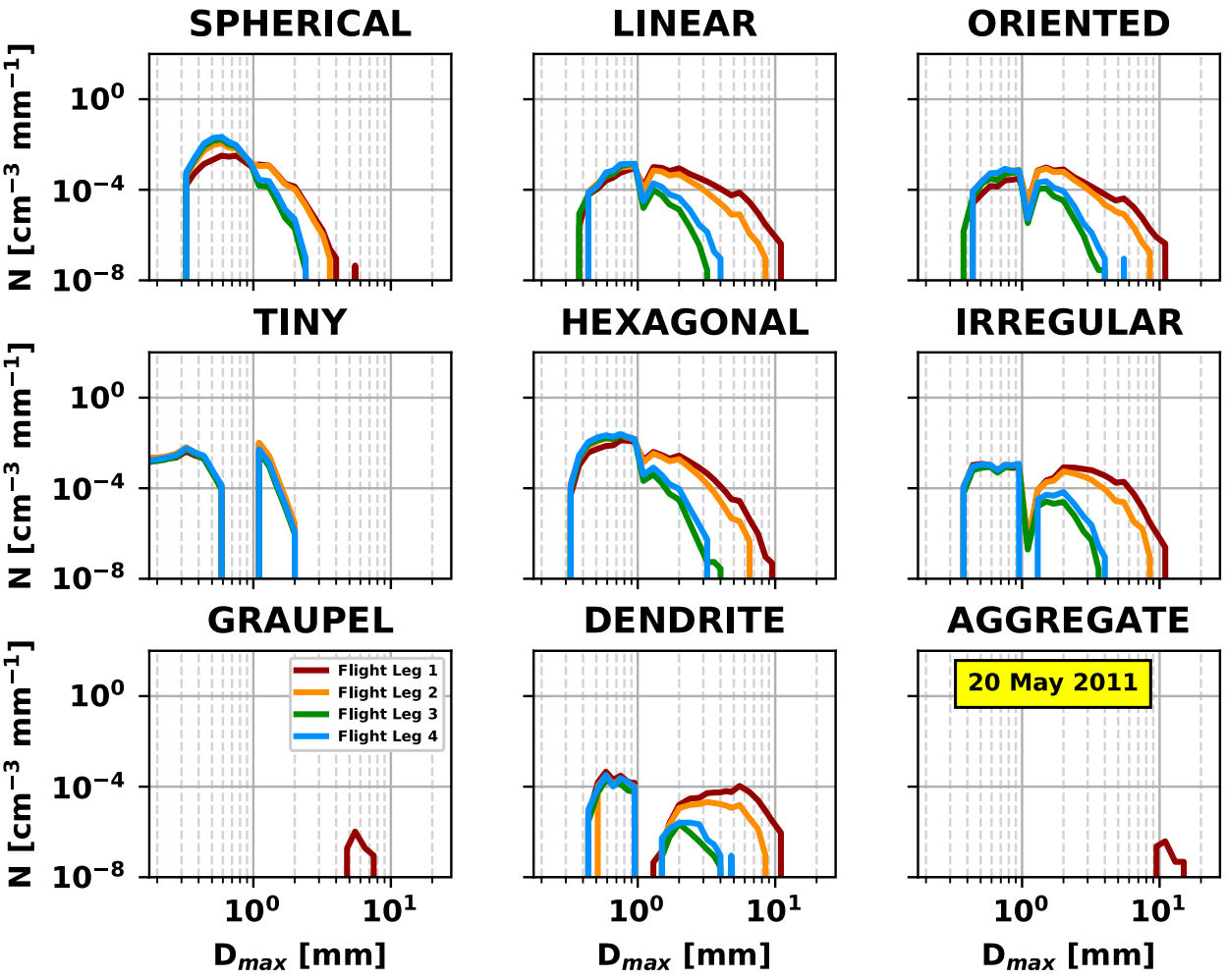

FIG. 3. The mean number distribution functions for nine particle habit classifications following the Holroyd (1987) classification scheme for each analyzed flight leg during the 20 May 2011 flight. The behavior of the number distribution functions between 1 and 2 mm is due to the coarse pixel resolution of the HVPS (as noted in the text), but insignificant given that 95% of the total mass for each flight leg is contained in the 2D-C measurements.

variability for the 20 May trailing stratiform case, likely owing to a having less temperature dependence in the higher-altitude anvil cirrus region (as in the 23 May case) compared to the lower-altitude trailing stratiform region of an MCS (also see Heymsfield et al. 2007). A similar methodology is developed here for characterizing uncertainty in $V(D)$ coefficients in the next section.

c. *Uncertainty estimates*

To compute uncertainties in V_T and hence V_M and V_Z, a χ^2 technique similar to those outlined above is described here. The χ^2 statistic, χ^2_V hereafter, minimized to determine (α, β) coefficients is represented as

$$\chi^2_V = \frac{1}{N}\sum_{i=1}^{N}[V_{\text{diff}}(i)], \tag{10}$$

where V_{diff} is a metric describing a weighted difference between the "best estimate" V_M or V_Z and that computed from $V(D)$ for a variety of (α, β), with the summation over N 10-s averaged data points along a given flight path. Here

$$V_{\text{diff}} = \left[\frac{V_{M;Z} - V_{M;Z,\text{SD}}(\alpha,\beta)}{\sqrt{V_{M;Z} \times V_{M;Z,\text{SD}}(\alpha,\beta)}}\right]^2, \tag{11}$$

$$V_{M,\text{SD}} = \frac{\sum_{i=1}^{K} \alpha D_i^{\beta}[m(D_i)]N(D_i)dD}{\sum_{i=1}^{K}[m(D_i)]N(D_i)dD}, \tag{12}$$

and

$$V_{Z,\text{SD}} = \frac{\sum_{i=1}^{K} \alpha D_i^{\beta}[m(D_i)]^2N(D_i)dD}{\sum_{i=1}^{K}[m(D_i)]^2N(D_i)dD}. \tag{13}$$

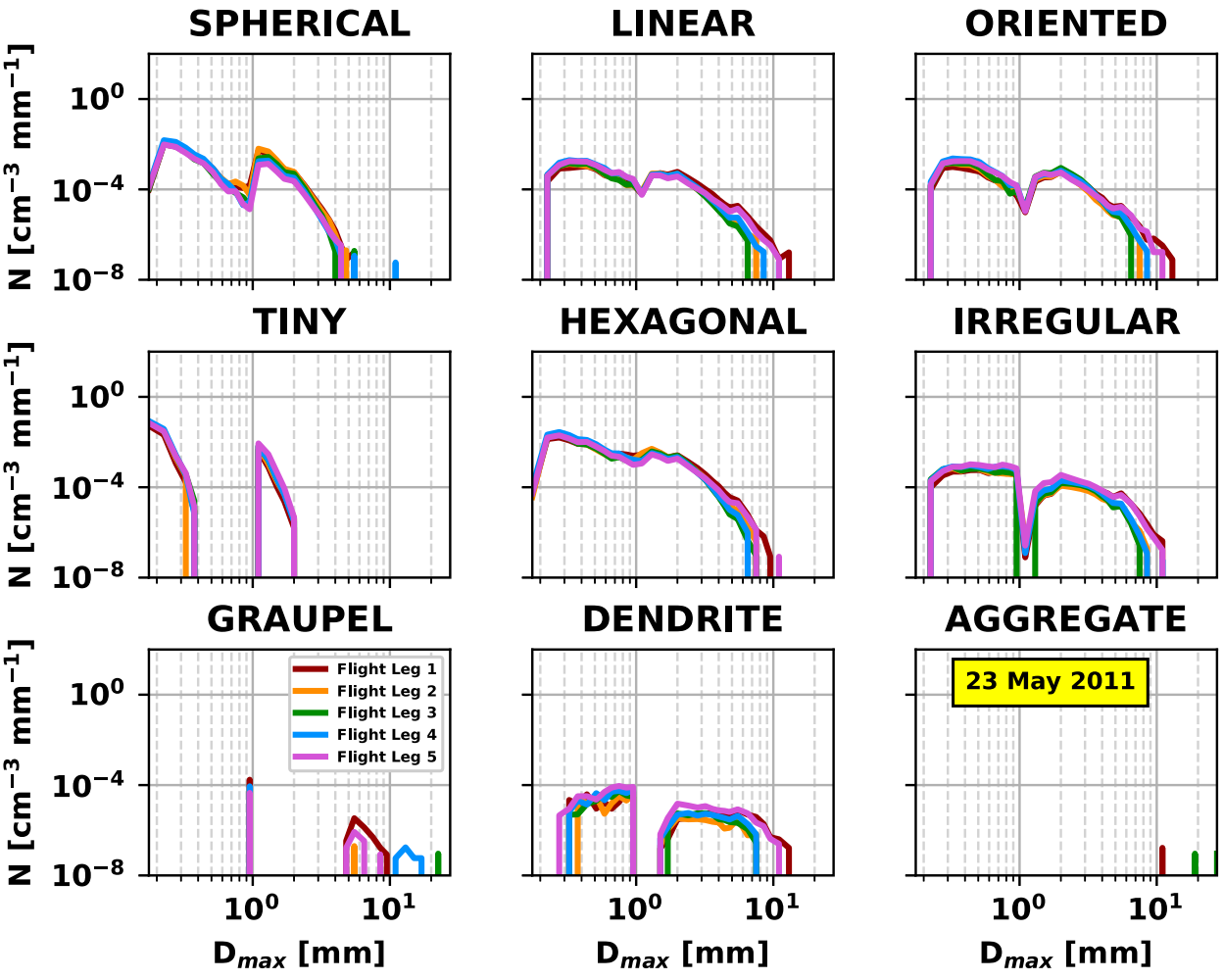

FIG. 4. As in Fig. 3, but for 23 May 2011 flight.

Equation (11) represents a weighted difference between the best estimate mass- or reflectivity-weighted mean fall velocity and the mean fall velocity derived from $N(D)$ and a given set of (α, β) coefficients. Note that V_M or V_Z is used in Eq. (11) depending upon whether mass- or reflectivity-weighted fall speeds are computed (hereafter, $V_{M;Z,\mathrm{SD}}$ refers to either $V_{M,\mathrm{SD}}$ or $V_{Z,\mathrm{SD}}$). The best estimates of both α and β are determined by finding the smallest χ^2_V. Given uncertainties, a range of α and β are equally possible in addition to the smallest χ^2_V. Thus, it is necessary to define a "tolerance" for χ^2_V such that any (α, β) value fulfilling $\chi^2_V < \chi^2_{\min} + \Delta\chi^2_V$ implies an "equally plausible" solution where $\chi^2_{\min}$ is the minimum χ^2_V determined from the best estimate of (α, β). This $\chi^2_{\min}$ represents natural parameter variability, which represents the expected variance in fall velocity due to variance in ice microphysical properties in similar environmental conditions (McFarquhar et al. 2015). The confidence region for χ^2_V is adapted here following McFarquhar et al. (2015) and Finlon et al. (2019), and defined as

$$\Delta\chi^2_V = \max(\chi^2_{\min}, \Delta\chi^2_{1,V}, \Delta\chi^2_{2,V}, \Delta\chi^2_{3,V}) \tag{14}$$

where $\Delta\chi^2_{1,V}$ represents uncertainties due to area ratio (A_r) measurements, $\Delta\chi^2_2$ represents uncertainties in maximum dimension ($D_{\max}$) estimates, and $\Delta\chi^2_3$ represents sampling uncertainties in particle size distributions.

The $\Delta\chi^2_{1,V}$ accounting for the uncertainty in A_r is given by

$$\Delta\chi^2_{1,V} = \frac{1}{N}\sum\left[\frac{V_{M,Z;V_t A_r \max}(i) - V_{M,Z}(i)}{\sqrt{V_{M,Z;V_t A_r \max}(i) \times V_{M,Z}(i)}}\right]^2, \tag{15}$$

where $V_{M,Z;V_t A_r \max}$ is the mean mass- or reflectivity-weighted fall velocity using the Best number X as in Eq. (5). The "max" annotation clarifies that A_r [i.e., Eq. (5) or the MI96 method] will almost always be larger than A_r^k [i.e., the corrected A_r following Eq. (6)] though it is noted that values of A_r can exceed 1 due to measurement error (especially for smaller particles).

The $\Delta\chi^2_{2,V}$ term accounts for the uncertainty in (α, β) owing to uncertainty in $D_{\max}$. Khvorostyanov and Curry (2002) showed using their ice particle fall velocity parameterization that (α, β) varies with $D_{\max}$ and particle habit, and Ding et al. (2020)

recently demonstrated that the surface of equally plausible (a, b) characterizing $M(D)$ relationships depends on $D_{\max}$ as well. It is possible that a similar dependence between $D_{\max}$ and the surface of equally plausible (α, β) in $V(D)$ relationships also exists via the uncertainty in $D_{\max}$. Thus, the $\Delta\chi^2_{2,V}$ term accounts for the dependence of (α, β) on $D_{\max}$ and is expressed as

$$\Delta\chi^2_{2,V} = \frac{1}{N}\sum\frac{1}{2}\left[\frac{V_{M,Z;V_tD\text{bin\_min}}(i) - V_{M,Z}(i)}{V_{M,Z;V_tD\text{bin\_min}}(i) \times V_{M,Z}(i)}\right]^2 + \frac{1}{2}\left[\frac{V_{M,Z;V_tD\text{bin\_max}}(i) - V_{M,Z}(i)}{V_{M,Z;V_tD\text{bin\_max}}(i) \times V_{M,Z}(i)}\right]^2, \quad (16)$$

with $V_{M,Z;V_tD\text{bin\_min}}$ and $V_{M,Z;V_tD\text{bin\_max}}$ representing the mean mass- or reflectivity-weighted fall velocities recomputed using the minimum/maximum endpoints of each bin [i.e., $D_i \pm \Delta D_i/2$]. The bin widths are used to proxy an uncertainty for $D_{\max}$, and therefore note that future studies should instead use $D_{\max}$ uncertainties once they become available for OAPs.

Finally, the uncertainty of $N(D)$ must also be accounted for when calculating $\Delta\chi^2_V$. Statistical sampling and measurement uncertainty make up two sources of uncertainty in $N(D)$. To account for statistical sampling uncertainty, $V_{M,Z}$ are recomputed by adding or subtracting the square root of the number of counts in each bin from the best estimate of $N(D)$ for that bin, analogous to Hallett (2003), McFarquhar et al. (2015), and Finlon et al. (2019), to give the uncertainty in total particle counts for each size bin consistent with Poisson statistics. The measurement uncertainty is assumed to be ±50% $N(D)$, based on Heymsfield et al. (2013). Thus, $\Delta\chi^2_{3,V}$ is written

$$\Delta\chi^2_{3,V} = \frac{1}{N}\sum\left(\frac{1}{2}\left\{\left[\frac{V_{M,Z;\text{SD}_{\min}}(i) - V_{M,Z;\text{SD}}(i)}{\sqrt{V_{M,Z;\text{SD}_{\min}}(i) \times V_{M,Z;\text{SD}}(i)}}\right]^2 + \left[\frac{V_{M,Z;\text{SD}_{\max}}(i) - V_{M,Z;\text{SD}}(i)}{\sqrt{V_{M,Z;\text{SD}_{\max}}(i) \times V_{M,Z;\text{SD}}(i)}}\right]^2\right\} + \frac{1}{2}\left\{\left[\frac{V_{M,Z;\text{meas}_{\min}}(i) - V_{M,Z}(i)}{V_{M,Z;\text{meas}_{\min}}(i) \times V_{M,Z}(i)}\right]^2 + \left[\frac{V_{M,Z;\text{meas}_{\max}}(i) - V_{M,Z}(i)}{V_{M,Z;\text{meas}_{\max}}(i) \times V_{M,Z}(i)}\right]^2\right\}\right). \quad (17)$$

In Eq. (17), $V_{M,Z;\text{SD}_{\max}}$ and $V_{M,Z;\text{SD}_{\min}}$ represent the mass- or reflectivity-weighted fall velocity computed using ±50% of the $N(D)$, respectively, following Heymsfield et al. (2013). For the remainder of this analysis, it is assumed all uncertainties are uncorrelated since each estimate is obtained from independent measurements. Quantifying these sources of uncertainty in the minimization of χ^2_V enables a direct comparison of the relative importance of A_r, $D_{\max}$, and $N(D)$ uncertainties on the computation of α and β. While $\Delta\chi^2_{3,V}$ was thought to be important, it was found that $\Delta\chi^2_{3,V}$ was near zero and hence not discussed further in this work. Understanding how these uncertainties affect α and β is important for refining fall velocity representation in models, for understanding fall velocity variation with environmental conditions, and for future improvements of cloud microphysics parameterization schemes.

The design and application of this methodology considers key sources of uncertainty *and* is flexible for future adaptation when, for example, measurements of airborne ice particle velocity may become available or a new source of uncertainty is identified. Thus, application of this methodology here can be regarded as a "proof of concept," and in comparing χ^2_T with χ^2_Z, the results of this study should be considered only in context of the sources of uncertainty.

4. Variability arising from equally plausible $M(D)$

a. Method

To evaluate how equally plausible (a, b) parameters in mass–dimension relations affect variability in $V(D)$ relationships, it is assumed that all equally plausible (a, b) can be used to represent $M(D)$ in Eqs. (12) and (13). All equally plausible $M(D)$ are used with all α between 0.05 and 25 $\text{m}^{1-\beta}\,\text{s}^{-1}$ (in increments of 0.025 $\text{m}^{1-\beta}\,\text{s}^{-1}$) and β between 0.05 and 0.85 (in increments of 0.0125) following Eqs. (12) and (13). For each (α, β) pair, the resulting $V_{M,Z;\text{SD}}$ is compared against $V_{M,Z}$ using a two-sided Student's t test. It is assumed that $V_{M,Z;\text{SD}}$ and $V_{M,Z}$ are statistically different if $p < 0.1$. Using this approach offers insight into *how many* and *what fraction* of equally plausible $M(D)$ can reproduce $V_{M,Z;\text{SD}}$ that are statistically similar to $V_{M,Z}$. Finally, the mean habit classification is also considered for this analysis. The mean habit classification is defined as the percentage of total mass for a given habit relative to the cumulative ice mass estimated by the 2D-C and HVPS probes. It is again noted that the 2D-C accounts for 95% of the total mass or more per flight segment, since HVPS data are only included for $D > 1$ mm in the composite PSD.

b. Results

Following the computations in section 3a and the methodology presented in section 4a, Fig. 5 reveals the percentage of equally plausible $M = aD^b_{\max}$ relations that produce a statistically similar distribution of $V = \alpha D^\beta_{\max}$ to each respective best estimate V_M across all 20 May 2011 flight legs. Table 3 shows the minimized $M(D)$ relationship as well as the mean flight leg velocity (V_M) used to generate each respective subplot in Fig. 5. The first flight leg for 20 May 2011 occurred in the warmest conditions (−5.9°C) among the nine flight legs examined. Despite all four flight legs for 20 May 2011 having habit frequencies to within 4% for a given habit (Table 2),

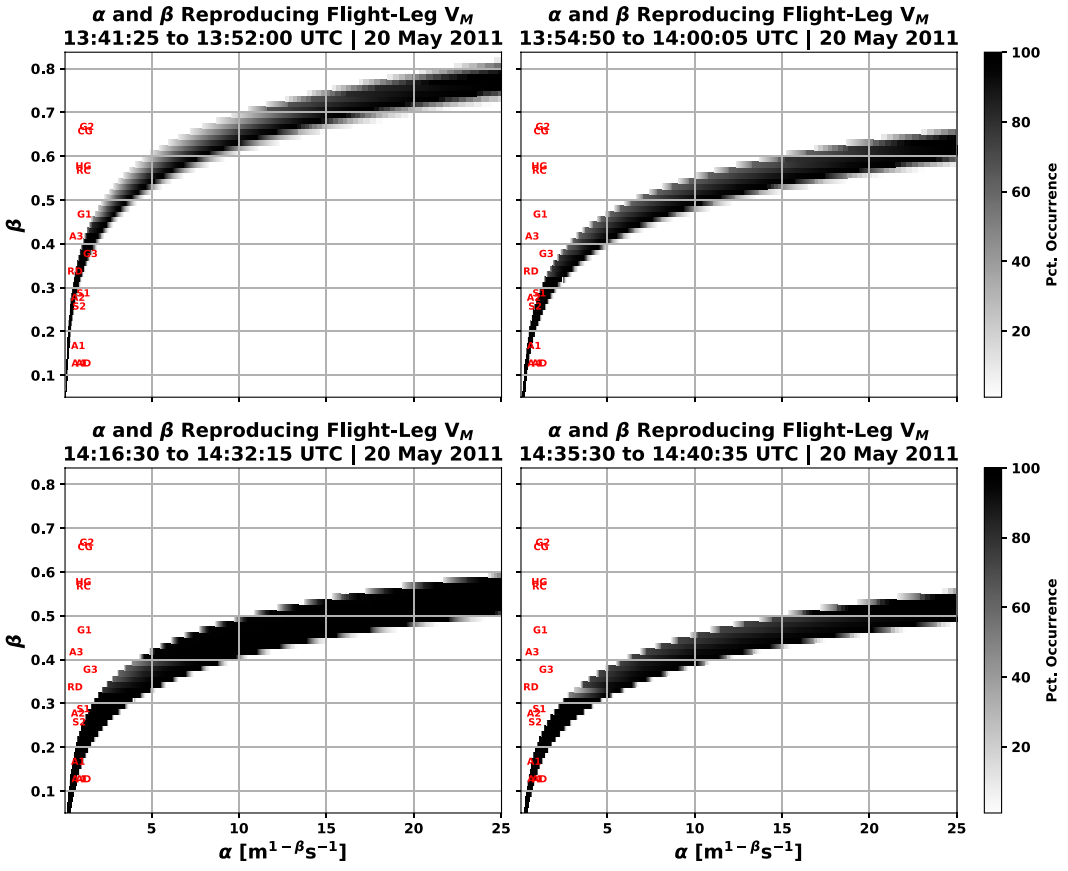

FIG. 5. Percentage of equally plausible (a, b) coefficients generated using all equally plausible $M(D)$ respective to each individual flight leg that provides statistically similar fall velocity to the 10-s averaged flight leg, best-estimate mass-weighted fall velocity V_M. Each of the red two-letter symbols represent the (α, β) pairs for habit classifications listed in Locatelli and Hobbs (1974) for reference (see Table 4 for more information).

Fig. 3 shows that flight leg 1 had the highest mean $N(D)$ for non-tiny and spherical habit particles with $D > 1$ mm. The habit frequencies are quite similar among the flight legs even though the HVPS habit distributions between flight legs 1 and 2 have lower mean $D_{\max}$ compared to flight legs 3 and 4. Flight legs 1 and 2 also took place at higher temperatures compared to flight legs 3 and 4 (see Table 2). The observed habit distributions likely result in flight leg 1 having the lowest a coefficient and lowest variability in a among the four flights leg on this day (Table 3), which is also consistent with the lowest V_M for all flight legs occurring during the first flight (see Fig. 1). Flight legs 2, 3, and 4 have lower β relative to α compared to flight leg 1 for all given α values, which is consistent with the observed ice particles having a higher mean

TABLE 3. Mean and standard deviation of 1-s, mass-weighted terminal velocities (left), best estimate $M(D)$ using Nevzorov probe TWC and WSR-88D radar reflectivity measurements (middle), and best estimate $M(D)$ using only radar reflectivity measurements for all flight legs on 20 May 2011 and 23 May 2011. The units of a are g cm^{-b}.

Flight segment	V_M (m s^{-1})	Minimized $M(D)$ (TWC + REFL)	Minimized $M(D)$ (REFL only)
1341:25–1352:00 UTC 20 May 2011	0.06 ± 0.01	a = 0.0050, b = 2.75	a = 0.0015, b = 1.10
1354:05–1400:05 UTC 20 May 2011	0.13 ± 0.02	a = 0.0100, b = 2.75	a = 0.0025, b = 1.55
1416:32–1432:15 UTC 20 May 2011	0.17 ± 0.06	a = 0.0265, b = 2.95	a = 0.0005, b = 1.10
1435:30–1440:35 UTC 20 May 2011	0.21 ± 0.05	a = 0.0115, b = 2.55	a = 0.0040, b = 1.95
2149:55–2155:15 UTC 23 May 2011	0.12 ± 0.04	a = 0.0055, b = 2.65	a = 0.0010, b = 1.30
2206:45–2211:00 UTC 23 May 2011	0.18 ± 0.04	a = 0.0010, b = 1.05	a = 0.0010, b = 1.05
2232:50–2237:15 UTC 23 May 2011	0.19 ± 0.06	a = 0.0020, b = 1.95	a = 0.0010, b = 1.35
2241:35–2248:20 UTC 23 May 2011	0.24 ± 0.07	a = 0.0035, b = 2.30	a = 0.0055, b = 2.85
2258:40–2303:40 UTC 23 May 2011	0.20 ± 0.09	a = 0.0020, b = 1.70	a = 0.0025, b = 2.50

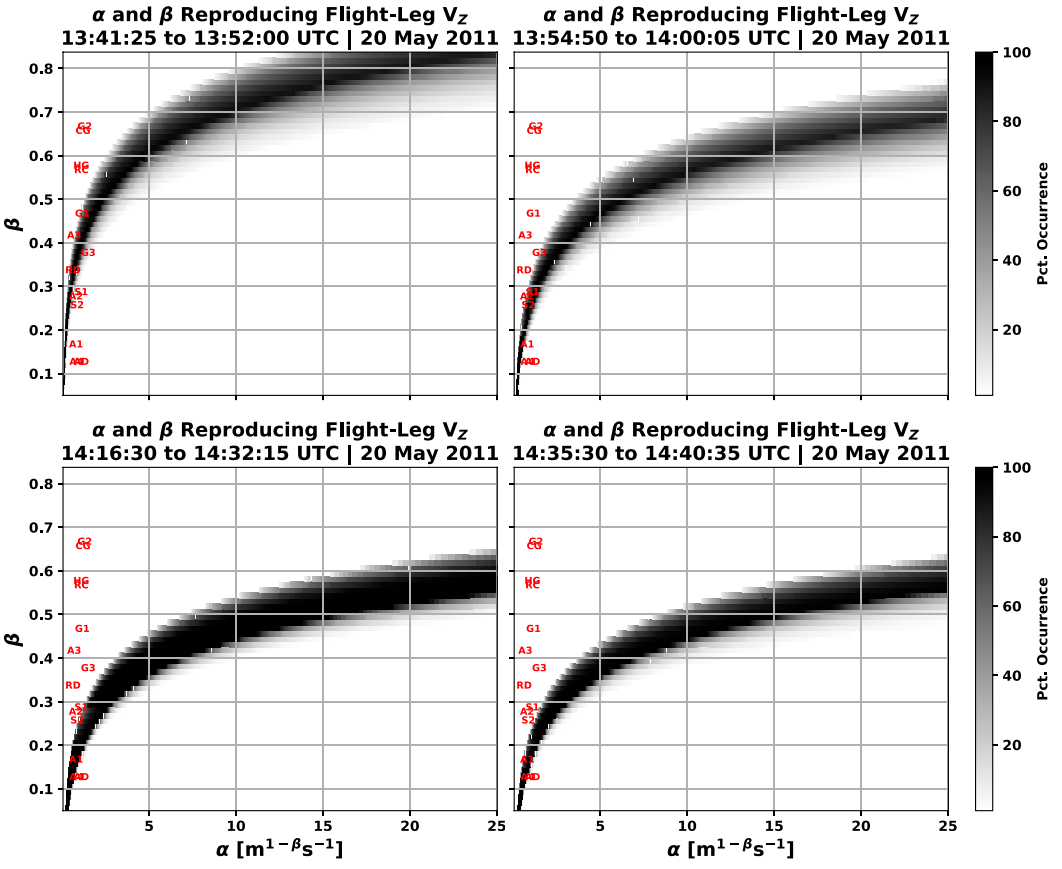

FIG. 6. As in Fig. 5, but for the 10-s averaged flight leg, best estimate reflectivity-weighted fall velocity V_Z.

mass or density (not shown). By contrast, these three flight legs have larger mean V_M and more variability in V_M (Fig. 1, Table 3) yet the spread in β only ranges from 0.45 to 0.70 for α between 20 and 25 $m^{1-\beta}\ s^{-1}$. These results alone do not fully disentangle *why* β values for given α vary differently for the first flight leg relative to the other three flight legs.

Figure 6 shows the percentage of equally plausible $M(D)$ that result in statistically similar flight leg V_Z for the given (α, β) ranges in section 4a. Reflectivity-weighted velocity uniformly results in β that are as much as 0.2 higher for given α relative to the results in Fig. 5 for V_M. The V_Z for the first flight leg on 20 May 2011 highlights this best: given that reflectivity weighting is proportional to the square of the particle mass (since Rayleigh scattering can be assumed for S-band radars), the greater contribution of larger particles to the total mass particles should explain the increase of β. For example, β is greater than 0.65 for α between 20 and 25 $m^{1-\beta}\ s^{-1}$ for the first flight leg whereas β was between 0.35 and 0.60 for α between 20 and 25 $m^{1-\beta}\ s^{-1}$ for the last three flight legs. Furthermore, the edges of the surfaces show that 40%–90% of equally plausible $M(D)$ solutions result in a statistically similar flight leg V_Z, compared to 80%–100% of equally plausible $M(D)$ solutions resulting in a statistically similar flight leg V_M. It is worth noting that there are far more equally plausible $M(D)$ for reflectivity-only data, where 7 of the 9 total flight legs contain more equally plausible $M(D)$ from the reflectivity-only weighting procedure (see column 2 in Table 5) compared to the joint mass and reflectivity weighting procedure. These results suggest that incorporating both mass and reflectivity measurements into the minimization procedure results in a more certain range of (α, β) for given conditions (Fig. 5), whereas a reflectivity-only-based procedure produces a wider, less certain range of (α, β) (Fig. 6). This is as the use of two constraints should better limit the range of variables.

For equally plausible V_M surfaces during the 23 May 2011 flight legs (Fig. 7), ranges of β in general are ~0.01–0.02 (0.05) larger for $\alpha < 5\ m^{1-\beta}\ s^{-1}$ ($\alpha > 20\ m^{1-\beta}\ s^{-1}$) compared to the equally plausible V_Z surfaces. By comparison, equally plausible V_Z surfaces (Fig. 8) cover noticeably larger areas compared to the 20 May 2011 flight legs (see Fig. 6) and to the equally plausible V_M surfaces for the 23 May 2011 flight legs. Over 50% of all ice mass observed by the 2D-C and HVPS for the 23 May 2011 flight legs were from ice particles classified as "tiny" (i.e., having fewer than 25 pixels). For the flight on 23 May 2011, radar reflectivity (denoted Z hereafter) was between 15 and 25 dBZ for all flight legs (see Fig. 6 in Finlon et al. 2019) whereas the 20 May 2011 flight had more variability with Z between 10 and 30 dBZ. The Z values observed during the first two flight legs on 20 May 2011 are higher overall because of the much larger observed ice particle concentrations, in

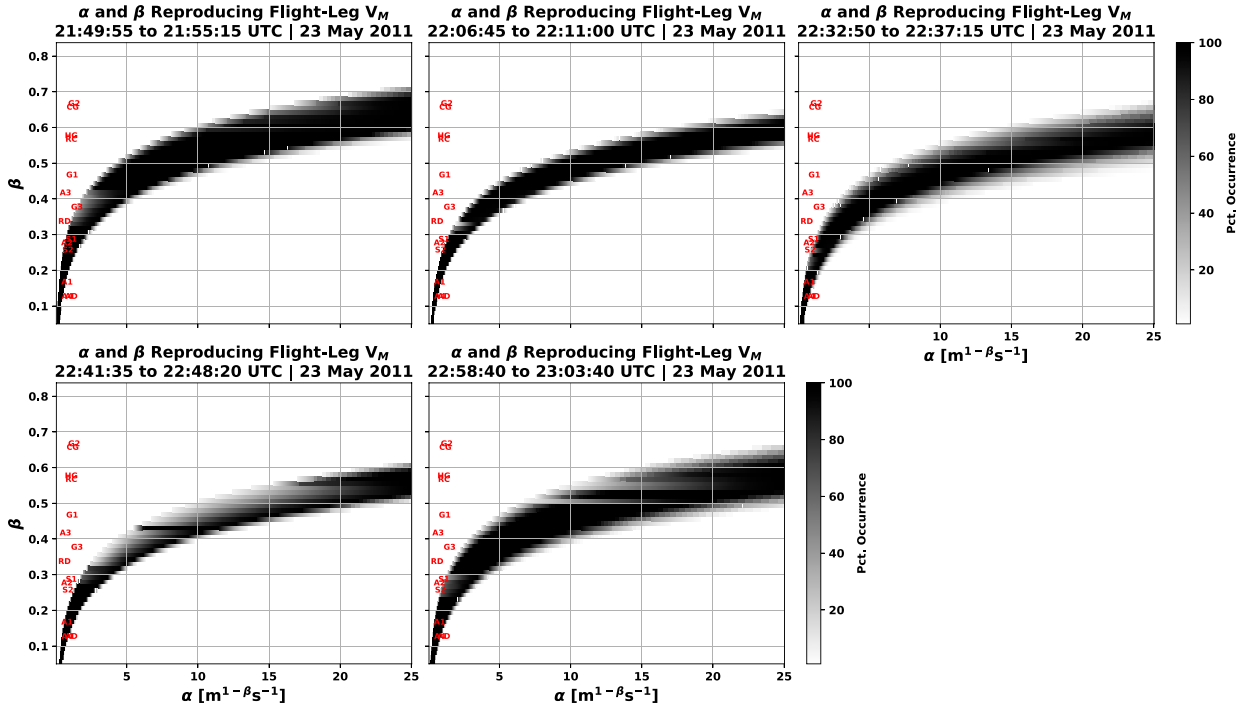

FIG. 7. As in Fig. 5, but for 23 May 2011 flight legs.

addition to larger maximum dimension particles (see Fig. 11 in Finlon et al. 2019). Furthermore, the ice water content (IWC) observed by the Nevzorov probe frequently measured between 0.5 and 1 g m^{-3} across all flight legs for 23 May 2011, as compared to 20 May 2011 when the total IWC measured between 0.5 and 0.7 g m^{-3} for only the first two flight legs (see Fig. 6 in Finlon et al. 2019). Thus, it is hypothesized that the increased variability in (α, β) for the 23 May 2011

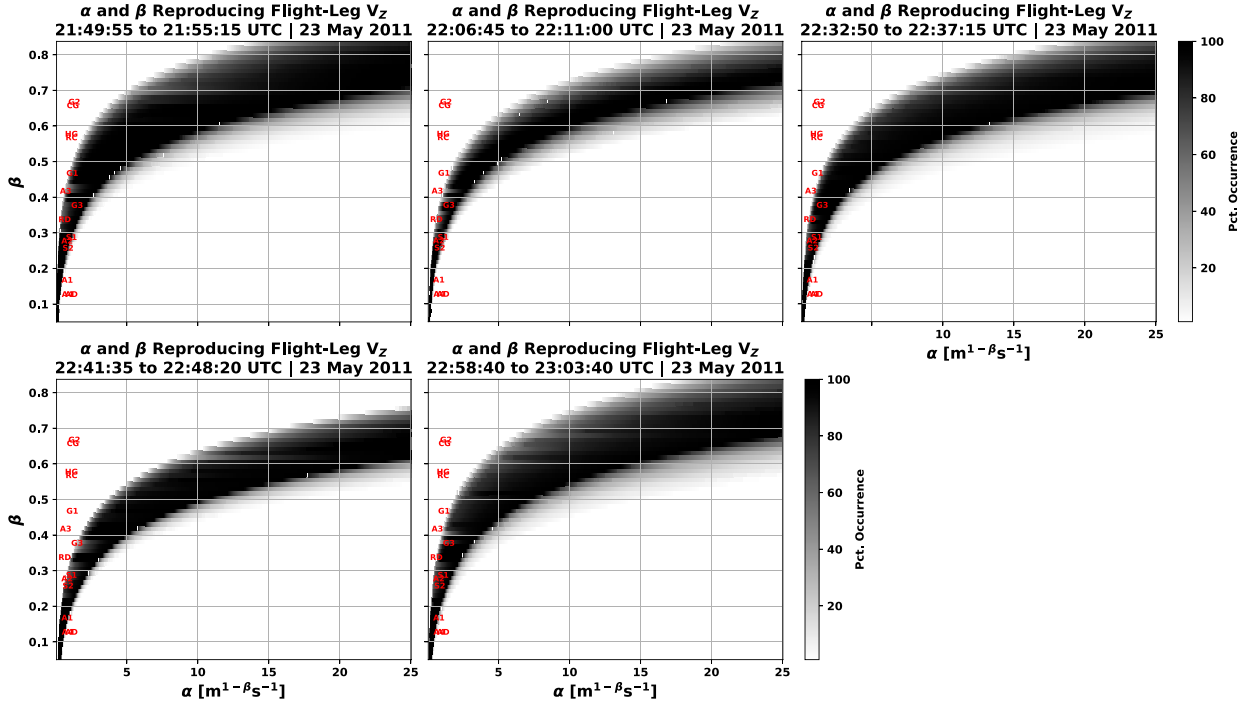

FIG. 8. As in Fig. 6, but for 23 May 2011 flight legs.

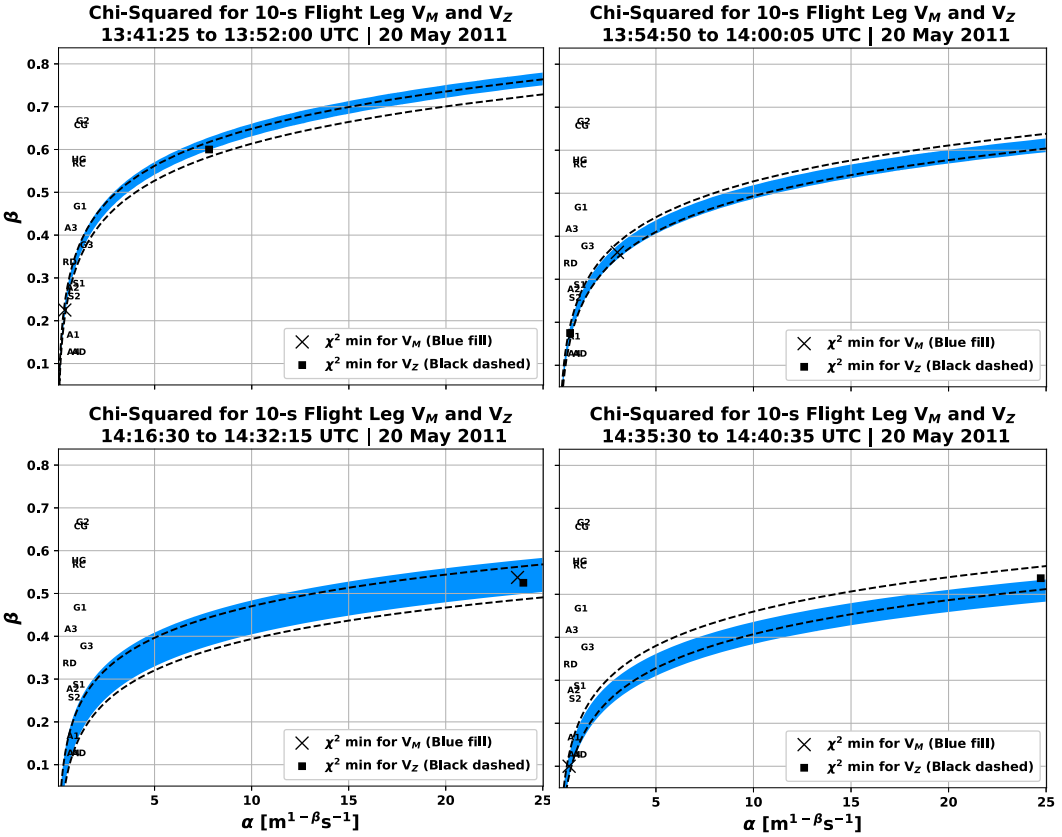

FIG. 9. Surfaces of equally plausible (α, β) coefficients generated using minimized $M(D)$ for each individual flight leg that accounts for uncertainty in area ratio, maximum dimension, and $N(D)$ in V_M (blue shading) and V_Z (black dashed) for 20 May 2011 flight legs. The × and square markers denote, respectively, the most likely (α, β) pair for V_M and V_Z. Each of the two-letter symbols represent the (α, β) pairs for habit classifications listed in Locatelli and Hobbs (1974) for reference (see Table 4 for more information).

flight legs results from larger mass associated with higher $N(D)$ at smaller size ranges especially when the total number concentration is dominated by ice particles less than 200 μm but IWC exceeds 0.5 g m^{-3}.

There are a couple of possible explanations why equally plausible $M(D)$ derived using combined mass and reflectivity measurements vary less than those derived using reflectivity only, as deduced by the areal coverage by the reflectivity-only surfaces in Figs. 6 and 8 compared to the combined surfaces in Figs. 5 and 7, especially for the 23 May 2011 flight legs. Temperature for the 20 May 2011 flight varied from −5.6° to −22.7°C as the aircraft sampled evolving conditions within a trailing stratiform region, but for five flight legs on 23 May 2011 only between −25.0° and −34.7°C when the anvil cirrus did not evolve as dramatically. Even though the IWC was consistently above 0.5 g m^{-3} on 23 May 2011, the ice particles much more frequently had $D < 200$ μm. This resulted in a higher β for all given α. The possibility also exists that the difference in minimized $M(D)$ using mass and reflectivity, compared to reflectivity only, is due to the limitation in the Nevzorov probe being unable to capture the largest particles where radar reflectivity is most sensitive to the largest ice particles in a given sample volume. In section 5, the equally plausible framework introduced in section 3 is used to elucidate how temperature and parameter variability affect ranges of equally plausible (α, β) surfaces.

5. Variability arising from A_r, D_{max}, and $N(D)$

Following the minimization procedures in section 3c, which accounts for variability arising from A_r, D_{max}, and $N(D)$, Fig. 9 shows surfaces of χ^2_V for the 20 May 2011 flight legs. Similar to Fig. 5, the resulting surfaces of equally plausible (α, β) for flight leg 1 are smallest in area and feature the highest β for all values of α compared to the other three flight legs. This is consistent with the best estimate V_M for this flight leg having the lowest variability (see Table 3). For all flight legs, the surface of equally plausible (α, β) using the mass-weighting routine overlaps at least 62% of the (α, β) surfaces using the reflectivity-weighting routine. Flight legs 1 and 3 have mass-weighted (α, β) surfaces where values of β are about 0.01 higher for all α compared to the reflectivity-weighted (α, β) surfaces, which contrasts the results detailed in section 4 showing that the reflectivity-weighted (α, β) surfaces have consistently larger β

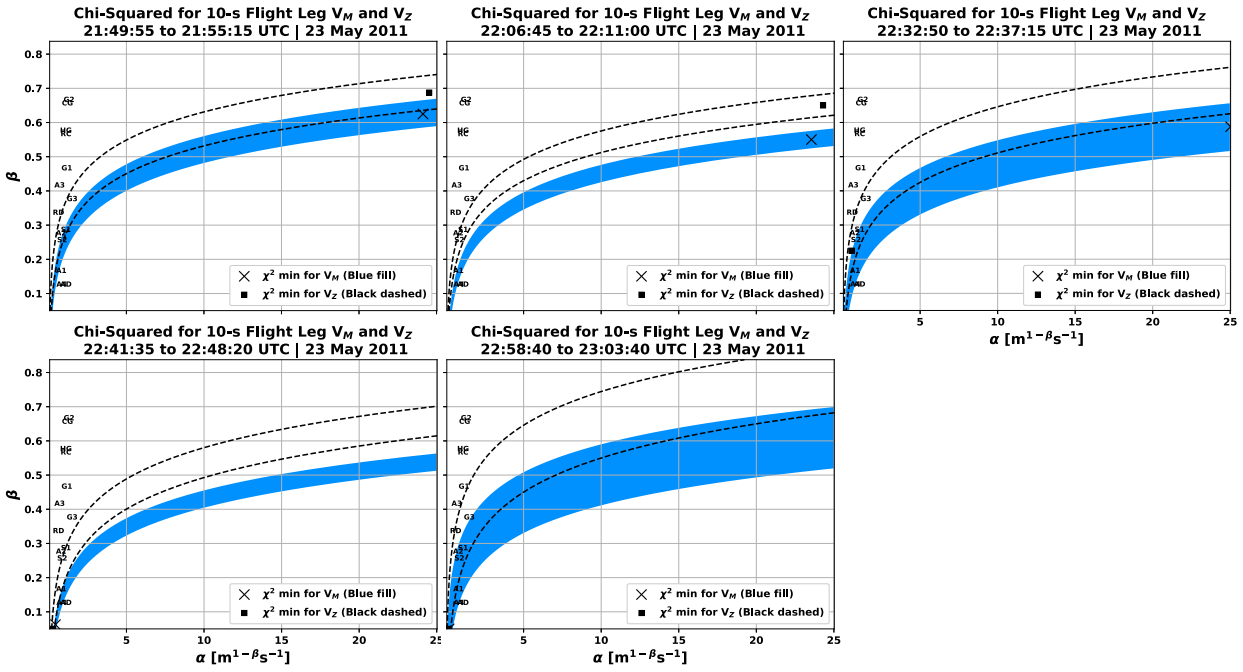

FIG. 10. As in Fig. 9, but for 23 May 2011 flight legs.

for all given α. This is not the case for the 23 May 2011 flight legs, where the reflectivity-weighted results for all five flight legs feature reflectivity-weighted (α, β) surfaces that have little overlap with the mass-weighted (α, β) surfaces (Fig. 10). In fact, there is no overlap between the mass- and reflectivity-weighted (α, β) surfaces for flight legs 2 and 4 on 23 May 2011. This is interesting because neither IWC nor radar reflectivity between these five flight legs are statistically different (result not shown). However, these flight legs are the only two legs among both flights where $\chi^2_{\min}$ for V_M is less than $\Delta\chi^2_{1,V}$, implying that uncertainty in A_r is larger than the natural parameter variability as well as uncertainties from $D_{\max}$ and $N(D)$ (see Table 5). This is also true for flight leg 3 on 23 May 2011 where $\chi^2_{\min}$ for V_Z is less than $\Delta\chi^2_{1,V}$, although the V_M surface overlaps approximately 29% of the V_Z (α, β) surfaces despite $\chi^2_{\min}$ for V_M or V_Z not falling within this overlapping surface. The main implication of this result is that, for flight legs occurring at temperatures less than −20°C, choosing between mass and reflectivity weighting may significantly affect the resulting set of equally plausible (α, β) surfaces. One possible explanation for this result is that temperatures less than −20°C favor higher density ice particles, making the results more sensitive to the choice of weighting (see Figs. 14 and 15 in Finlon et al. 2019). In fact, when comparing these results to specific (α, β) pairs derived by Locatelli and Hobbs (1974) for individual habits, at least four pairs overlap for any given surface (see Table 5). Note, however, that most of these $V(D)$ relationships were derived for ice particles with maximum dimensions between 1 and 3 mm and their coefficients were not adjusted to sea level for proper comparison with other environments or studies. Further research is needed to evaluate our equally plausible framework against $V(D)$ relationships derived from ice particle datasets where a similar fraction of mass is contained in sub-1-mm maximum dimension ice particles.

Another interesting result is that the $\Delta\chi^2_{1,V}$ values for 23 May 2011 are approximately 5 times higher than $\Delta\chi^2_{1,V}$ values for 20 May 2011 (Table 5), showing that the uncertainty introduced by A_r increases when a greater fraction of mass is contained in smaller ($D < 200$ μm) ice particles (see Figs. 3 and 4). Further, higher-density ice particles such as bullet rosettes and columns form at lower temperatures (HW10) thus causing an increase in $\Delta\chi^2_{1,V}$. Given that smaller ice particles tend to dominate at these temperatures, it makes sense that the uncertainty arising from A_r exceeds that of natural parameter variability (i.e., $\chi^2_{\min}$) in these conditions. This also makes sense from a measurement perspective, because the 2D-C cross-sectional area becomes less accurate for smaller particles due to decreased image resolution for smaller ice particle maximum dimension (Heymsfield and Miloshevich 2003). Conversely, for the 20 May 2011 flight legs, uncertainty arising from $D_{\max}$ (i.e., $\Delta\chi^2_{2,V}$) becomes more important relative to uncertainty arising from A_r (i.e., $\Delta\chi^2_{1,V}$), with Table 4 showing that $\Delta\chi^2_{1,V}$ and $\Delta\chi^2_{2,V}$ are closer in magnitude. Although $\Delta\chi^2_{1,V}$ is slightly larger for all four 20 May 2011 flight legs compared to $\Delta\chi^2_{2,V}$ for both V_M and V_Z, both $\Delta\chi^2_{1,V}$ and $\Delta\chi^2_{2,V}$ are much less in magnitude than $\chi^2_{\min}$. The relatively larger $\chi^2_{\min}$ compared to $\Delta\chi^2_{1,V}$ and $\Delta\chi^2_{2,V}$ suggests that natural parameter variability between the assumed (α, β) and best estimate V_M and V_Z is more important for determining uncertainty in conditions such as the trailing stratiform conditions sampled in the four 20 May 2011 flight legs. The applicability of this conclusion to cloud properties in similar temperature regimes in

TABLE 4. List of $V(D) = \alpha D^{\beta}$ relationships from previous studies. Units of α are $m^{1-\beta}\ s^{-1}$; β is unitless.

Habit	Symbol (Fig. 10)	(α, β)	Reference
Lump graupel	G1	(1.16, 0.46)	Locatelli and Hobbs (1974)
	G2	(1.30, 0.66)	
	G3	(1.50, 0.37)	
Conical graupel	CG	(1.20, 0.65)	Locatelli and Hobbs (1974)
Hexagonal graupel	HG	(1.10, 0.57)	Locatelli and Hobbs (1974)
Graupel-like snow	S1	(1.10, 0.28)	Locatelli and Hobbs (1974)
	S2	(0.86, 0.25)	
(Rimed) columns	RC	(1.10, 0.56)	Locatelli and Hobbs (1974)
(Rimed) dendrites	RD	(0.62, 0.33)	Locatelli and Hobbs (1974)
(Rimed) assemblages of dendrites	AD	(1.10, 0.12)	Locatelli and Hobbs (1974)
Unrimed side planes	SP	(0.81, 0.99)	Locatelli and Hobbs (1974)
Aggregates	A1	(0.80, 0.16)	Locatelli and Hobbs (1974)
	A2	(0.79, 0.27)	
	A3	(0.69, 0.41)	
	A4	(0.82, 0.12)	

other temperature and geographic regimes would have to be tested using data from other airborne research flights, since only two research flights are analyzed here.

Comparison of Figs. 5–8 with Figs. 9 and 10 shows that using the most likely (a, b), without considering variability in (a, b), results in a smaller set of equally realizable (α, β). Noting that Fig. 6 incorporates the most likely (a, b) without considering the range of possible solutions, the resulting surfaces of equally plausible (α, β) for $V(D)$ relationships cover less area than the resulting surfaces shown in Figs. 5–8 where the range of plausible (a, b) is considered using both mass- and reflectivity-weighting schemes. Similar to Figs. 6 and 8, the surfaces of equally plausible (α, β) for the 23 May 2011 flight cover more area compared to the 20 May 2011 flight. For all reflectivity-weighted V_Z results, the (α, β) surfaces cover regions where β is as much as 0.1 less for a given α, irrespective of the total area covered by the (α, β) surfaces. If only reflectivity data are available, using a single $M(D)$ solution without considering the range of equally plausible (a, b) for $M(D)$ results in a larger equally plausible (α, β) surface for V_Z, implying increased uncertainty relative to V_M.

Overall, the findings presented in this study suggest that the most important sources of uncertainty vary with temperature. For example, for temperatures less than −20°C, $\Delta\chi^2_{1,V}$ (i.e., A_r) is much larger compared to $\Delta\chi^2_{2,V}$ (i.e., $D_{\max}$) and can exceed natural parameter variability (i.e., $\chi^2_{\min}$) as the leading source of uncertainty (see Table 5). Temperature can influence the primary ice particle habits in a given sample and, for example, environmental regimes conducive for columnar and needle shapes more likely to contribute to lower values of A_r,

TABLE 5. Total number of equally plausible (a, b) pairs for $M(D)$ relationships using a mass weighting procedure (χ^2_M) or a reflectivity weighting procedure (χ^2_Z). Also shown are minimized χ^2 statistics for all (α, β) surfaces ($\chi^2_{\min}$) and uncertainties in the area ratio ($\Delta\chi^2_{1,V}$), maximum dimension ($\Delta\chi^2_{2,V}$), and in the $N(D)$ ($\Delta\chi^2_{3,V}$).χ^2 statistics are shown for V_M (V_Z).

Flight segment	No. of $M(D)$ for χ^2_M (χ^2_Z)	$\chi^2_{\min}$	$\Delta\chi^2_{1,V}$	$\Delta\chi^2_{2,V}$	$\Delta\chi^2_{3,V}$
1341:25–1352:00 UTC 20 May 2011	39 (115)	0.013 55 (0.019 77)	0.008 26 (0.0073)	0.007 16 (0.007 10)	≪0.001 (≪0.001)
1354:05–1400:05 UTC 20 May 2011	100 (215)	0.018 25 (0.020 91)	0.008 80 (0.008 39)	0.007 56 (0.007 38)	≪ 0.001 (≪0.001)
1416:32–1432:15 UTC 20 May 2011	219 (386)	0.146 19 (0.141 85)	0.008 18 (0.00 803)	0.007 55 (0.007 42)	≪0.001 (≪0.001)
1435:30–1440:35 UTC 20 May 2011	45 (151)	0.060 27 (0.055 84)	0.008 08 (0.007 81)	0.007 68 (0.007 50)	≪0.001 (≪0.001)
2149:55–2155:15 UTC 23 May 2011	99 (90)	0.122 01 (0.200 02)	0.040 12 (0.025 75)	0.026 62 (0.020 16)	≪0.001 (≪0.001)
2206:45–2211:00 UTC 23 May 2011	182 (152)	0.030 73 (0.074 97)	0.049 26 (0.028 53)	0.031 48 (0.023 37)	≪0.001 (≪0.001)
2232:50–2237:15 UTC 23 May 2011	88 (95)	0.443 02 (0.351 35)	0.048 12 (0.039 36)	0.030 90 (0.026 73)	≪0.001 (≪0.001)
2241:35–2248:20 UTC 23 May 2011	28 (58)	0.041 72 (0.127 48)	0.049 82 (0.046 35)	0.031 59 (0.029 96)	≪0.001 (≪0.001)
2258:40–2303:40 UTC 23 May 2011	37 (59)	0.922 34 (0.718 81)	0.046 55 (0.042 36)	0.026 18 (0.024 15)	≪0.001 (≪0.001)

further influencing the Best or Davies number. Likewise, the overlap between the mass- and reflectivity-weighted surfaces was much less for the 20 May 2011 cases compared to 23 May 2011, which can be attributed to mean density differences in the ice particles sampled respective for each flight. By contrast for the 23 May 2011 case, the choice in mass or reflectivity weighting resulted in considerably more overlap in the equally plausible (α, β) surfaces compared to colder conditions sampled on 20 May 2011, and natural parameter variability was the largest source of uncertainty compared to A_r, $D_{\max}$, or $N(D)$. These results make clear that the key uncertainty source in ice particle velocity, as well as underlying results from choosing mass or reflectivity weighting, is highly dependent on the sampling environment and meteorology. Given the cloud particles examined in this work were convectively generated, there is a need to apply and test this methodology on nonconvectively generated ice clouds to clarify if any differences in uncertainty sources arise in varying meteorological regimes. For example, Hu et al. (2021) noted key differences in ice cloud properties as functions of their proximity to convective cores.

6. Conclusions

Two different approaches for quantifying uncertainty in ice particle fall velocity calculations were developed and evaluated. The first method addresses uncertainty in $V(D)$ relationships arising from equally realizable $M(D)$ relationships, and the second method establishes a framework for evaluating the relative roles of different sources of uncertainty in $V(D)$ relationships of the form $V(D) = \alpha D^{\beta}$ appropriate for use in models, including differences arising from weighting the fall speed by mass or reflectivity to derive the coefficients. All V_T were adjusted to SLP, such that all results were easily comparable to one another. The use of equally plausible (a, b) coefficients in $M(D) = aD^b$ relationships to determine surfaces of equally plausible (α, β) coefficients for $V(D)$ results in larger surfaces when using a reflectivity-weighting scheme (i.e., for V_Z) compared to a mass weighting scheme (i.e., for V_M) for two research flights during the Midlatitude Continental Clouds Experiment (MC3E). The uncertainties arising from variability of parameters [e.g., A_r, $D_{\max}$, and $N(D)$] used to compute ice particle fall velocity and those from the variability of the equally plausible $M(D)$ relationships were shown to not have as large of an impact as natural variability for constraining uncertainty in $V(D)$ relationships. The spread in β for any given α was lower for the trailing stratiform conditions sampled on 20 May 2011 compared to the 23 May 2011 flight legs. Further, the equally plausible (α, β) surfaces generated using V_M and V_Z had more overlap for all flight legs on 20 May 2011 compared to 23 May 2011.

Overall, results from our study suggest that

1) the most important source of uncertainty (i.e., natural parameter variability, A_r, or $D_{\max}$) changes relative to the ambient temperature,
2) additional studies need to consider measurements sampling more meteorological conditions at similar temperatures and altitudes, especially for stratiform clouds given that clouds sampled in this study were convectively generated, and
3) future studies should further account for how these parameters depend on other environmental variables like relative humidity.

Studies of fall velocity parameterizations are also limited by the fact that real measurements of fall velocity are currently unavailable from airborne platforms at flight level. The techniques developed here should also be applied to more detailed measurements of fall velocity available from ground-based remote sensing instruments where long-term V_T datasets can be collected or retrieved. As one example, ice particle fall velocity data could be retrieved from ground-based vertically pointing radar if the ambient atmospheric vertical velocity is known (e.g., Kollias et al. 2007; Shupe et al. 2008a,b). The Multi-Angle Snowflake Camera (Garrett et al. 2012) can also attain accurate ice particle fall speed data in light wind conditions and proper wind shielding (Fitch et al. 2021). Vázquez-Martín et al. (2021b) recently quantified ice particle mass from maximum dimension, cross-sectional area, and particle fall velocity from a recently developed dataset using the Dual Ice Crystal Imager (D-ICI; Kuhn and Vázquez-Martín 2020). The Multi-Angle Snowflake Camera and D-ICI dataset represent two viable datasets to consider for future studies investigating uncertainty in ice particle terminal velocities.

Future studies should investigate how surfaces of (α, β) coefficients vary in a wider variety of environmental conditions, such as tropical cyclones, winter storms, frontal systems, and other storm systems. Noting that severe hailstorms cause billions of dollars in damage worldwide each year (Changnon 1999), further constraint of ice particle fall velocities at the initial growth phase of hail could further improve model representations of hail evolution and subsequent application for evaluating a variety of newer, state-of-the-art hail retrievals and climatologies (e.g., Bang and Cecil 2019, 2021; Brook et al. 2021). More generally, improved constraints on ice particle fall velocities could lead to better forecasts and simulations of convective parameters such as lapse rates, mixing ratio, precipitation, and hail (e.g., Grabowski 1999; Lin et al. 2021), as well as potentially aid in identifying sources of systematic biases in model forecasts where atmospheric state reanalysis products are used as inputs (Van Weverberg et al. 2013; Gensini et al. 2014; Taszarek et al. 2020). Fall velocities for high IWC conditions (i.e., IWC > 0.5 g m^{-3}) should also be explored, especially given evidence presented here that overlap between mass- and reflectivity-weighted (α, β) surfaces decreases with increasing IWC. High IWC conditions were not uncommon during MC3E and occur frequently (e.g., Rugg et al. 2021; Hu et al. 2021). Ongoing work investigating the difference in equally plausible $M(D)$ relationships using the Nevzorov and Isokinetic Probe–2 (IKP-2; Strapp et al. 2016) may improve estimates of $V(D)$ relationships by reducing uncertainties apparent from Nevzorov IWC data, which

TABLE A1. List of variables and abbreviations used throughout this study.

Variable	Units	Description
$\Delta\chi^2_{1,V}$	—	Uncertainty in a $V(D)$ relationship attributed to A_r
$\Delta\chi^2_{2,V}$	—	Uncertainty in a $V(D)$ relationship attributed to maximum dimension
$\Delta\chi^2_{3,V}$	—	Uncertainty in a $V(D)$ relationship attributed to $N(D)$
A_r	—	Area ratio of an ice particle
R_e	—	Reynolds number
V_{diff}	m s^{-1}	Weighted difference between V_M and $V_{M,\text{SD}}$ (for mass weighting) and V_Z or $V_{Z,\text{SD}}$ (for reflectivity weighting)
$V_{M,\text{SD}}$	m s^{-1}	Mass-weighted, 10-s average fall velocity derived using $V(D) = \alpha D^{\beta}$, where α and β are varying
V_M	m s^{-1}	Mass-weighted, 10-s average fall velocity using best-estimate V_T data
V_T	m s^{-1}	Terminal fall velocity of an individual ice particle
$V_{Z,\text{SD}}$	m s^{-1}	Reflectivity-weighted, 10-s average fall velocity derived using $V(D) = \alpha D^{\beta}$, where α and β are varying
V_Z	m s^{-1}	Reflectivity-weighted, 10-s average fall velocity using best-estimate V_T data
X^*	—	Modified Best number, as in HW10
χ^2_{min}	—	Minimized χ^2 for a $M(D)$ or $V(D)$ relationship due to natural variability within the parameters
χ^2_T	—	Chi-squared statistic for determining the relative roles of natural variability and parameter variability for $M(D) = aD^b$ relationships, using both TWC and Z
χ^2_V	—	Chi-squared statistic for determining the relative roles of natural variability and parameter uncertainty in $V(D) = \alpha D^{\beta}$ relationships
χ^2_Z	—	Chi-squared statistic for determining the relative roles of natural variability and parameter variability for $M(D) = aD^b$ relationships, using only Z
D	mm	Maximum dimension of an ice particle
HW10	—	Abbreviation referencing the Heymsfield and Westbrook (2010) study
$M(D)$	g	Mass–dimension relationship
MI96		Abbreviation referencing the Mitchell (1996) study
$N(D)$	cm^{-3} mm^{-1}	Number distribution function, or number of particles for the bin centered at maximum dimension D
TWC	g m^{-3}	Total water content
$V(D)$	m s^{-1}	Velocity–dimension relationship
X	—	Best number, as in MI96
Z	mm^6 m^{-3}	Radar reflectivity factor

were used for equally plausible $M(D)$ relationships. Finally, our results showing variability in V_M or V_Z from varying (α, β) can be implemented in a stochastic framework in models (e.g., Stanford et al. 2019) using the P3 microphysical parameterization scheme to explore how uncertainties in fall velocity cascade up to model predicted V_M or V_Z and other fields.

Acknowledgments. We acknowledge colleagues within the CIWRO Cloud Physics Group for providing valuable comments, questions, and feedback about this work as well as John D'Alessandro, who provided a thorough review of the manuscript. We also acknowledge Hugh Morrison for his insightful and valuable comments, which improved the quality of this manuscript. We also acknowledge Wei Wu for his assistance with the UIOOPS software package. We appreciate the efforts of all who worked on the MC3E field campaign to collect a high-quality dataset. Finally, we would like to acknowledge the three anonymous reviewers who gave thorough and insightful comments leading to the improved quality of this manuscript. AD and GMM were supported by the office of Biological and Environmental Research (BER) of the U.S. Department of Energy Atmospheric Systems Research Program through Grant DE-SC0016476 (through UCAR Subcontract SUBAWD000397).

Data availability statement. The ice particle terminal velocity data used throughout this paper are archived online through the DOE ARM Data Discovery portal (DOI pending). All MC3E airborne data are publicly accessible via https://www.arm.gov/research/campaigns/aaf2011airborne. Matched aircraft and radar data used to compute the equally plausible $M(D)$ relationships for the 20 and 23 May 2011 MC3E case studies are publicly available at https://doi.org/10.13012/B2IDB-6396968_V1 (Finlon 2018).

APPENDIX

List of Variables and Abbreviations

Table A1 presents a list of variables and abbreviations used throughout this study.

REFERENCES

Afchine, A., and Coauthors, 2018: Ice particle sampling from aircraft—Influence of the probing position on the ice water content. *Atmos. Meas. Tech.*, **11**, 4015–4031, https://doi.org/10.5194/amt-11-4015-2018.

Bailey, M. P., and J. Hallett, 2009: A comprehensive habit diagram for atmospheric ice crystals: Confirmation from the laboratory, AIRS II, and other field studies. *J. Atmos. Sci.*, **66**, 2888–2899, https://doi.org/10.1175/2009JAS2883.1.

Baker, B., and R. P. Lawson, 2006: Improvement in determination of ice water content from two-dimensional particle imagery. Part I: Image-to-mass relationships. *J. Appl. Meteor. Climatol.*, **45**, 1282–1290, https://doi.org/10.1175/JAM2398.1.

Bang, S. D., and D. J. Cecil, 2019: Constructing a multifrequency passive microwave hail retrieval and climatology in the GPM domain. *J. Appl. Meteor. Climatol.*, **58**, 1889–1904, https://doi.org/10.1175/JAMC-D-19-0042.1.

——, and ——, 2021: Testing passive microwave-based hail retrievals using GPM DPR Ku-band radar. *J. Appl. Meteor. Climatol.*, **60**, 255–271, https://doi.org/10.1175/JAMC-D-20-0129.1.

Barrett, A. I., C. D. Westbrook, J. C. Nicol, and T. H. M. Stein, 2019: Rapid ice aggregation process revealed through triple-wavelength Doppler spectrum radar analysis. *Atmos. Chem. Phys.*, **19**, 5753–5769, https://doi.org/10.5194/acp-19-5753-2019.

Baumgardner, D., and A. Korolev, 1997: Airspeed corrections for optical array probe sample volumes. *J. Atmos. Oceanic Technol.*, **14**, 1224–1229, https://doi.org/10.1175/1520-0426(1997)014<1224:ACFOAP>2.0.CO;2.

——, and Coauthors, 2012: In situ, airborne instrumentation: Addressing and solving measurement problems in ice clouds. *Bull. Amer. Meteor. Soc.*, **93**, ES29–ES34, https://doi.org/10.1175/BAMS-D-11-00123.1.

Beard, K. V., 1980: The effects of altitude and electrical force on the terminal velocity of hydrometeors. *J. Atmos. Sci.*, **37**, 1363–1374, https://doi.org/10.1175/1520-0469(1980)037<1363:TEOAAE>2.0.CO;2.

Best, A. C., 1950: Empirical formulae for the terminal velocity of water drops falling through the atmosphere. *Quart. J. Roy. Meteor. Soc.*, **76**, 302–311, https://doi.org/10.1002/qj.49707632905.

Böhm, H. P., 1989: A general equation for the terminal fall speed of solid hydrometeors. *J. Atmos. Sci.*, **46**, 2419–2427, https://doi.org/10.1175/1520-0469(1989)046<2419:AGEFTT>2.0.CO;2.

Bony, S., C. Risi, and F. Vimeux, 2008: Influence of convective processes on the isotopic composition (δ^{18}O and δD) of precipitation and water vapor in the tropics: 1. Radiative-convective equilibrium and Tropical Ocean–Global Atmosphere–Coupled Ocean-Atmosphere Response Experiment (TOGA-COARE) simulations. *J. Geophys. Res.*, **113**, D19305, https://doi.org/10.1029/2008JD009942.

——, and Coauthors, 2015: Clouds, circulation and climate sensitivity. *Nat. Geosci.*, **8**, 261–268, https://doi.org/10.1038/ngeo2398.

Brandes, E. A., K. Ikeda, G. Thompson, and M. Schönhuber, 2008: Aggregate terminal velocity/temperature relations. *J. Appl. Meteor. Climatol.*, **47**, 2729–2736, https://doi.org/10.1175/2008JAMC1869.1.

Brook, J. P., A. Protat, J. Soderholm, J. T. Carlin, H. McGowan, and R. A. Warren, 2021: HailTrack—Improving radar-based hailfall estimates by modeling hail trajectories. *J. Appl. Meteor. Climatol.*, **60**, 237–254, https://doi.org/10.1175/JAMC-D-20-0087.1.

Brown, P. R. A., and P. N. Francis, 1995: Improved measurements of the ice water content in cirrus using a total-water probe. *J. Atmos. Oceanic Technol.*, **12**, 410–414, https://10.1175/1520-0426(1995)012<0410:IMOTIW>2.0.CO;2.

Bühl, J., P. Seifert, M. Radenz, H. Baars, and A. Ansmann, 2019: Ice crystal number concentration from lidar, cloud radar and radar wind profiler measurements. *Atmos. Meas. Tech.*, **12**, 6601–6617, https://doi.org/10.5194/amt-12-6601-2019.

Changnon, S. A., 1999: Data and approaches for determining hail risk in the contiguous United States. *J. Appl. Meteor.*, **38**, 1730–1739, https://doi.org/10.1175/1520-0450(1999)038<1730:DAAFDH>2.0.CO;2.

Chase, R. J., and Coauthors, 2018: Evaluation of triple-frequency radar retrieval of snowfall properties using coincident airborne in situ observations during OLYMPEX. *Geophys. Res. Lett.*, **45**, 5752–5760, https://doi.org/10.1029/2018GL077997.

——, S. W. Nesbitt, and G. M. McFarquhar, 2021: A dual-frequency radar retrieval of two parameters of the snowfall particle size distribution using a neural network. *J. Appl. Meteor. Climatol.*, **60**, 341–359, https://doi.org/10.1175/JAMC-D-20-0177.1.

D'Alessandro, J. J., M. Diao, C. Wu, X. Liu, J. B. Jensen, and B. B. Stephens, 2019: Cloud phase and relative humidity distributions over the Southern Ocean in austral summer based on in situ observations and CAM5 simulations. *J. Climate*, **32**, 2781–2805, https://doi.org/10.1175/JCLI-D-18-0232.1.

Daloz, A. S., E. Nelson, T. L'Ecuyer, A. D. Rapp, and L. Sun, 2018: Assessing the coupled influences of clouds on the atmospheric energy and water cycles in reanalyses with A-Train observations. *J. Climate*, **31**, 8241–8264, https://doi.org/10.1175/JCLI-D-17-0862.1.

Davies, C. N., 1945: Definitive equations for the fluid resistance of spheres. *Proc. Phys. Soc.*, **57**, 259–270, https://doi.org/10.1088/0959-5309/57/4/301.

Ding, S., G. M. McFarquhar, S. W. Nesbitt, R. J. Chase, M. R. Poellot, and H. Wang, 2020: Dependence of mass–dimensional relationships on median mass diameter. *Atmosphere*, **11**, 756, https://doi.org/10.3390/atmos11070756.

Dzambo, A. M., and D. D. Turner, 2016: Characterizing relative humidity with respect to ice in midlatitude cirrus clouds as a function of atmospheric state. *J. Geophys. Res. Atmos.*, **121**, 12 253–12 269, https://doi.org/10.1002/2015JD024643.

Erfani, E., and D. L. Mitchell, 2017: Growth of ice particle mass and projected area during riming. *Atmos. Chem. Phys.*, **17**, 1241–1257, https://doi.org/10.5194/acp-17-1241-2017.

Faber, S., J. R. French, and R. Jackson, 2018: Laboratory and in-flight evaluation of measurement uncertainties from a commercial Cloud Droplet Probe (CDP). *Atmos. Meas. Tech.*, **11**, 3645–3659, https://doi.org/10.5194/amt-11-3645-2018.

Finlon, J. A., 2018: Matched radar and microphysical properties during MC3E. Illinois Data Bank, accessed 13 February 2021, https://doi.org/10.13012/B2IDB-6396968_V1.

——, G. M. McFarquhar, S. W. Nesbitt, R. M. Rauber, H. Morrison, W. Wu, and P. Zhang, 2019: A novel approach for characterizing the variability in mass–dimension relationships: Results from MC3E. *Atmos. Chem. Phys.*, **19**, 3621–3643, https://doi.org/10.5194/acp-19-3621-2019.

——, and Coauthors, 2020: Structure of an atmospheric river over Australia and the Southern Ocean: II. Microphysical evolution. *J. Geophys. Res. Atmos.*, **125**, e2020JD032514, https://doi.org/10.1029/2020JD032514.

Fitch, K. E., C. Hang, A. Talaei, and T. J. Garrett, 2021: Arctic observations and numerical simulations of surface wind effects on Multi-Angle Snowflake Camera measurements. *Atmos. Meas. Tech.*, **14**, 1127–1142, https://doi.org/10.5194/amt-14-1127-2021.

Garrett, T. J., C. Fallgatter, K. Shkurko, and D. Howlett, 2012: Fall speed measurement and high-resolution multi-angle photography of hydrometeors in free fall. *Atmos. Meas. Tech.*, **5**, 2625–2633, https://doi.org/10.5194/amt-5-2625-2012.

Gensini, V. A., T. L. Mote, and H. E. Brooks, 2014: Severe-thunderstorm reanalysis environments and collocated radiosonde observations. *J. Appl. Meteor. Climatol.*, **53**, 742–751, https://doi.org/10.1175/JAMC-D-13-0263.1.

Grabowski, W. W., 1999: A parameterization of cloud microphysics for long-term cloud-resolving modeling of tropical convection. *Atmos. Res.*, **52**, 17–41, https://doi.org/10.1016/S0169-8095(99)00029-0.

Hallett, J., 2003: *Handbook of Weather, Climate, and Water*. John Wiley and Sons, 973 pp., https://doi.org/10.1002/0471721603.

Helmus, J., and S. Collis, 2016: The Python ARM Radar Toolkit (Py-ART), a library for working with weather radar data in the Python programming language. *J. Open Res. Software*, **4**, e25, https://doi.org/10.5334/jors.119.

Heymsfield, A., 1972: Ice crystal terminal velocities. *J. Atmos. Sci.*, **29**, 1348–1357, https://doi.org/10.1175/1520-0469(1972)029<1348:ICTV>2.0.CO;2.

——, and L. M. Miloshevich, 2003: Parameterizations for the cross-sectional area and extinction of cirrus and stratiform ice cloud particles. *J. Atmos. Sci.*, **60**, 936–956, https://doi.org/10.1175/1520-0469(2003)060<0936:PFTCSA>2.0.CO;2.

——, and C. D. Westbrook, 2010: Advances in the estimation of ice particle fall speeds using laboratory and field measurements. *J. Atmos. Sci.*, **67**, 2469–2482, https://doi.org/10.1175/2010JAS3379.1.

——, A. R. Jameson, and H. W. Frank, 1980: Hail growth mechanisms in a Colorado storm: Part II: Hail formation processes. *J. Atmos. Sci.*, **37**, 1779–1807, https://doi.org/10.1175/1520-0469(1980)037<1779:HGMIAC>2.0.CO;2.

——, A. Bansemer, P. R. Field, S. L. Durden, J. Stith, J. E. Dye, W. Hall, and T. Grainger, 2002: Observations and parameterizations of particle size distributions in deep tropical cirrus and stratiform precipitating clouds: Results from in situ observations in TRMM field campaigns. *J. Atmos. Sci.*, **59**, 3457–3491, https://doi.org/10.1175/1520-0469(2002)059<3457:OAPOPS>2.0.CO;2.

——, ——, C. Schmitt, C. Twohy, and M. R. Poellot, 2004: Effective ice particle densities derived from aircraft data. *J. Atmos. Sci.*, **61**, 982–1003, https://doi.org/10.1175/1520-0469(2004)061<0982:EIPDDF>2.0.CO;2.

——, ——, and C. H. Twohy, 2007: Refinements to ice particle mass dimensional and terminal velocity relationships for ice clouds. Part I: Temperature dependence. *J. Atmos. Sci.*, **64**, 1047–1067, https://doi.org/10.1175/JAS3890.1.

——, C. Schmitt, and A. Bansemer, 2013: Ice cloud particle size distributions and pressure-dependent terminal velocities from in situ observations at temperatures from 0° to −86°C. *J. Atmos. Sci.*, **70**, 4123–4154, https://doi.org/10.1175/JAS-D-12-0124.1.

Hofer, S., A. J. Tedstone, X. Fettweis, and J. L. Bamber, 2019: Cloud microphysics and circulation anomalies in future Greenland melt. *Nat. Climate Change*, **9**, 523–528, https://doi.org/10.1038/s41558-019-0507-8.

Hogan, R. J., M. P. Mittermaier, and A. J. Illingworth, 2006: The retrieval of ice water content from radar reflectivity factor and temperature and its use in evaluating a mesoscale model. *J. Appl. Meteor. Climatol.*, **45**, 301–317, https://doi.org/10.1175/JAM2340.1.

Holroyd, E. W., III, 1987: Some techniques and uses of 2D-C habit classification software for snow particles. *J. Atmos. Oceanic Technol.*, **4**, 498–511, https://doi.org/10.1175/1520-0426(1987)004<0498:STAUOC>2.0.CO;2.

Hu, Y., and Coauthors, 2021: Dependence of ice microphysical properties on environmental parameters: Results from HAIC-HIWC Cayenne field campaign. *J. Atmos. Sci.*, **78**, 2957–2981, https://doi.org/10.1175/JAS-D-21-0015.1.

Huang, Y., and Coauthors, 2021: Microphysical processes producing high ice water contents (HIWCs) in tropical convective clouds during the HAIC-HIWC field campaign: Evaluation of simulations using bulk microphysical schemes. *Atmos. Chem. Phys.*, **21**, 6919–6944, https://doi.org/10.5194/acp-21-6919-2021.

Jackson, R. C., G. M. McFarquhar, J. Stith, M. Beals, R. A. Shaw, J. Jensen, J. Fugal, and A. Korolev, 2014: An assessment of the impact of antishattering tips and artifact removal techniques on cloud ice size distributions measured by the 2D cloud probe. *J. Atmos. Oceanic Technol.*, **31**, 2567–2590, https://doi.org/10.1175/JTECH-D-14-00018.1.

Jensen, A. A., J. Y. Harrington, H. Morrison, and J. A. Milbrandt, 2017: Predicting ice shape evolution in a bulk microphysics model. *J. Atmos. Sci.*, **74**, 2081–2104, https://doi.org/10.1175/JAS-D-16-0350.1.

Jensen, E. J., and Coauthors, 2013: Ice nucleation and dehydration in the tropical tropopause layer. *Proc. Natl. Acad. Sci. USA*, **110**, 2041–2046, https://doi.org/10.1073/pnas.1217104110.

——, and Coauthors, 2017: The NASA Airborne Tropical Tropopause Experiment: High-altitude aircraft measurements in the tropical western Pacific. *Bull. Amer. Meteor. Soc.*, **98**, 129–143, https://doi.org/10.1175/BAMS-D-14-00263.1.

Jensen, M. P., and Coauthors, 2015: The Midlatitude Continental Convective Clouds Experiment (MC3E) sounding network: Operations, processing and analysis. *Atmos. Meas. Tech.*, **8**, 421–434, https://doi.org/10.5194/amt-8-421-2015.

——, and Coauthors, 2016: The Midlatitude Continental Convective Clouds Experiment (MC3E). *Bull. Amer. Meteor. Soc.*, **97**, 1667–1686, https://doi.org/10.1175/BAMS-D-14-00228.1.

Kajikawa, M., 1973: Laboratory measurement of falling velocity of individual ice crystals. *J. Meteor. Soc. Japan*, **51**, 263–272, https://doi.org/10.2151/jmsj1965.51.4_263.

Khvorostyanov, V. I., and J. A. Curry, 2002: Terminal velocities of droplets and crystals: Power laws with continuous parameters over the size spectrum. *J. Atmos. Sci.*, **59**, 1872–1884, https://doi.org/10.1175/1520-0469(2002)059<1872:TVODAC>2.0.CO;2.

——, and ——, 2005: Fall velocities of hydrometeors in the atmosphere: Refinements to a continuous analytical power law. *J. Atmos. Sci.*, **62**, 4343–4357, https://doi.org/10.1175/JAS3622.1.

Klein, S. A., and C. Jakob, 1999: Validation and sensitivities of frontal clouds simulated by the ECMWF model. *Mon. Wea. Rev.*, **127**, 2514–2531, https://doi.org/10.1175/1520-0493(1999)127<2514:VASOFC>2.0.CO;2.

Kollias, P., E. E. Clothiaux, M. A. Miller, B. A. Albrecht, G. L. Stephens, and T. P. Ackerman, 2007: Millimeter-wavelength radars: New frontier in atmospheric cloud and precipitation research. *Bull. Amer. Meteor. Soc.*, **88**, 1608–1624, https://doi.org/10.1175/BAMS-88-10-1608.

Korolev, A. V., J. W. Strapp, G. A. Isaac, and A. N. Nevzorov, 1998: The Nevzorov airborne hot-wire LWC–TWC probe: Principle of operation and performance characteristics. *J. Atmos. Oceanic Technol.*, **15**, 1495–1510, https://doi.org/10.1175/1520-0426(1998)015<1495:TNAHWL>2.0.CO;2.

——, E. Emery, J. Strapp, S. Cober, G. Isaac, M. Wasey, and D. Marcotte, 2011: Small ice particles in tropospheric clouds: Fact or artifact? Airborne Icing Instrumentation Evaluation experiment. *Bull. Amer. Meteor. Soc.*, **92**, 967–973, https://doi.org/10.1175/2010BAMS3141.1.

Krämer, M., and Coauthors, 2016: A microphysics guide to cirrus clouds—Part 1: Cirrus types. *Atmos. Chem. Phys.*, **16**, 3463–3483, https://doi.org/10.5194/acp-16-3463-2016.

Kuhn, T., and S. Vázquez-Martín, 2020: Microphysical properties and fall speed measurements of snow ice crystals using the Dual Ice Crystal Imager (D-ICI). *Atmos. Meas. Tech.*, **13**, 1273–1285, https://doi.org/10.5194/amt-13-1273-2020.

Lin, L., Q. Fu, X. Liu, Y. Shan, S. E. Giangrande, G. S. Elsaesser, K. Yang, and D. Wang, 2021: Improved convective ice microphysics parameterization in the NCAR CAM model. *J. Geophys. Res. Atmos.*, **126**, e2020JD034157, https://doi.org/10.1029/2020JD034157.

List, R., and R. S. Schemenauer, 1971: Free-fall behavior of planar snow crystals, conical graupel and small hail. *J. Atmos. Sci.*, **28**, 110–115, https://doi.org/10.1175/1520-0469(1971)028<0110:FFBOPS>2.0.CO;2.

Locatelli, J. D., and P. V. Hobbs, 1974: Fall speeds and masses of solid precipitation particles. *J. Geophys. Res.*, **79**, 2185–2197, https://doi.org/10.1029/JC079i015p02185.

Magee, N., and Coauthors, 2021: Captured cirrus ice particles in high definition. *Atmos. Chem. Phys.*, **21**, 7171–7185, https://doi.org/10.5194/acp-21-7171-2021.

Mascio, J., Z. Xu, and G. G. Mace, 2017: The mass-dimensional properties of cirrus clouds during TC4. *J. Geophys. Res. Atmos.*, **122**, 10 402–10 417, https://doi.org/10.1002/2017JD026787.

Matrosov, S. Y., and A. J. Heymsfield, 2000: Use of Doppler radar to assess ice cloud particle fall velocity-size relations for remote sensing and climate studies. *J. Geophys. Res.*, **105**, 22 427–22 436, https://doi.org/10.1029/2000JD900353.

McFarquhar, G. M., and A. J. Heymsfield, 1996: Microphysical characteristics of three anvils sampled during the Central Equatorial Pacific Experiment. *J. Atmos. Sci.*, **53**, 2401–2423, https://doi.org/10.1175/1520-0469(1996)053<2401:MCOTAS>2.0.CO;2.

——, and R. A. Black, 2004: Observations of particle size and phase in tropical cyclones: Implications for mesoscale modeling of microphysical processes. *J. Atmos. Sci.*, **61**, 422–439, https://doi.org/10.1175/1520-0469(2004)061<0422:OOPSAP>2.0.CO;2.

——, A. J. Heymsfield, A. Macke, J. Iaquinta, and S. M. Aulenbach, 1999: Use of observed ice crystal sizes and shapes to calculate mean-scattering properties and multispectral radiances: CEPEX April 4, 1993, case study. *J. Geophys. Res.*, **104**, 31 763–31 779, https://doi.org/10.1029/1999JD900802.

——, H. Zhang, G. Heymsfield, J. B. Halverson, R. Hood, J. Dudhia, and F. Marks Jr., 2006: Factors affecting the evolution of Hurricane Erin (2001) and the distributions of hydrometeors: Role of microphysical processes. *J. Atmos. Sci.*, **63**, 127–150, https://doi.org/10.1175/JAS3590.1.

——, J. Um, M. Freer, D. Baumgardner, G. L. Kok, and G. Mace, 2007: Importance of small ice crystals to cirrus properties: Observations from the Tropical Warm Pool International Cloud Experiment (TWP-ICE). *Geophys. Res. Lett.*, **34**, L13803, https://doi.org/10.1029/2007GL029865.

——, T.-L. Hsieh, M. Freer, J. Mascio, and B. F. Jewett, 2015: The characterization of ice hydrometeor gamma size distributions as volumes in N_0–μ–λ phase space: Implications for microphysical process modeling. *J. Atmos. Sci.*, **72**, 892–909, https://doi.org/10.1175/JAS-D-14-0011.1.

——, and Coauthors, 2017: Processing of ice cloud in situ data collected by bulk water, scattering, and imaging probes: Fundamentals, uncertainties, and efforts toward consistency. *Ice Formation and Evolution in Clouds and Precipitation: Measurement and Modeling Challenges*, *Meteor. Monogr.*, No. 58, Amer. Meteor. Soc., https://doi.org/10.1175/AMSMONOGRAPHS-D-16-0007.1.

——, J. A. Finlon, D. M. Stechman, W. Wu, R. C. Jackson, and M. Freer, 2018: University of Illinois/Oklahoma Optical Array Probe (OAP) processing software, version 3.1.4. Zenodo, https://doi.org/10.5281/zenodo.1285969.

Milbrandt, J. A., H. Morrison, D. T. Dawson II, and M. Paukert, 2021: A triple-moment representation of ice in the Predicted Particle Properties (P3) microphysics scheme. *J. Atmos. Sci.*, **78**, 439–458, https://doi.org/10.1175/JAS-D-20-0084.1.

Mitchell, D. L., 1996: Use of mass- and area-dimensional power laws for determining precipitation particle terminal velocities. *J. Atmos. Sci.*, **53**, 1710–1723, https://doi.org/10.1175/1520-0469(1996)053<1710:UOMAAD>2.0.CO;2.

——, R. Zhang, and R. L. Pitter, 1990: Mass-dimensional relationships for ice particles and the influence of riming on snowfall rates. *J. Appl. Meteor. Climatol.*, **29**, 153–163, https://doi.org/10.1175/1520-0450(1990)029<0153:MDRFIP>2.0.CO;2.

——, P. Rasch, D. Ivanova, G. McFarquhar, and T. Nousiainen, 2008: Impact of small ice crystal assumptions on ice sedimentation rates in cirrus clouds and GCM simulations. *Geophys. Res. Lett.*, **35**, L09806, https://doi.org/10.1029/2008GL033552.

Morrison, H., and J. A. Milbrandt, 2015: Parameterization of cloud microphysics based on the prediction of bulk ice particle properties. Part I: Scheme description and idealized tests. *J. Atmos. Sci.*, **72**, 287–311, https://doi.org/10.1175/JAS-D-14-0065.1.

——, and Coauthors, 2020: Confronting the challenge of modeling cloud and precipitation microphysics. *J. Adv. Model. Earth Syst.*, **12**, e2019MS001689, https://doi.org/10.1029/2019MS001689.

Nakaya, U., and T. Terada, 1935: Simultaneous observations of the mass, falling velocity and form of individual snow crystals. *J. Fac. Sci. Hokkaido Univ. Ser. 2*, **1**, 191–201.

Nelson, E. L., and T. S. L'Ecuyer, 2018: Global character of latent heat release in oceanic warm rain systems. *J. Geophys. Res. Atmos.*, **123**, 4797–4817, https://doi.org/10.1002/2017JD027844.

Nesbitt, S., N. Guy, T. Lang, A. Lyons, and J. Finlon, 2019: Airborne Weather Observation Toolkit (AWOT), version 0.2.13. Zenodo, https://doi.org/10.5281/ZENODO.2587168.

Nettesheim, J. J., and P. K. Wang, 2018: A numerical study on the aerodynamics of freely falling planar ice crystals. *J. Atmos. Sci.*, **75**, 2849–2865, https://doi.org/10.1175/JAS-D-18-0041.1.

Rugg, A., J. Haggerty, and A. Protat, 2021: Global and regional patterns in high ice water content conditions. *J. Appl. Meteor. Climatol.*, **60**, 141–155, https://doi.org/10.1175/JAMC-D-20-0163.1.

Sanderson, B. M., C. Piani, W. J. Ingram, D. A. Stone, and M. R. Allen, 2008: Toward constraining climate sensitivity by linear analysis of feedback patterns in thousands of perturbed-physics GCM simulations. *Climate Dyn.*, **30**, 179–190, https://doi.org/10.1007/s00382-007-0280-7.

Schmitt, C. G., and A. J. Heymsfield, 2010: The dimensional characteristics of ice crystal aggregates from fractal geometry. *J. Atmos. Sci.*, **67**, 1605–1616, https://doi.org/10.1175/2009JAS3187.1.

——, K. Sulia, Z. J. Lebo, A. J. Heymsfield, V. Przybyo, and P. Connolly, 2019: The fall speed variability of similarly sized ice particle aggregates. *J. Appl. Meteor. Climatol.*, **58**, 1751–1761, https://doi.org/10.1175/JAMC-D-18-0291.1.

Shates, J. A., C. Pettersen, T. S. L'Ecuyer, S. J. Cooper, M. S. Kulie, and N. B. Wood, 2021: High-latitude precipitation: Snowfall regimes at two distinct sites in Scandinavia. *J. Appl. Meteor. Climatol.*, **60**, 1127–1148, https://doi.org/10.1175/JAMC-D-20-0248.1.

Shupe, M. D., and Coauthors, 2008a: A focus on mixed-phase clouds. *Bull. Amer. Meteor. Soc.*, **89**, 1549–1562, https://doi.org/10.1175/2008BAMS2378.1.

——, P. Kollias, M. Poellot, and E. Eloranta, 2008b: On deriving vertical air motions from cloud radar Doppler spectra. *J. Atmos. Oceanic Technol.*, **25**, 547–557, https://doi.org/10.1175/2007JTECHA1007.1.

Sledd, A., and T. L'Ecuyer, 2021: Uncertainty in forced and natural arctic solar absorption variations in CMIP6 models. *J. Climate*, **34**, 931–948, https://doi.org/10.1175/JCLI-D-20-0244.1.

Spichtinger, P., and M. Krämer, 2013: Tropical tropopause ice clouds: A dynamic approach to the mystery of low crystal numbers. *Atmos. Chem. Phys.*, **13**, 9801–9818, https://doi.org/10.5194/acp-13-9801-2013.

Stanford, M. W., A. Varble, E. Zipser, J. W. Strapp, D. Leroy, A. Schwarzenboeck, R. Potts, and A. Protat, 2017: A ubiquitous ice size bias in simulations of tropical deep convection. *Atmos. Chem. Phys.*, **17**, 9599–9621, https://doi.org/10.5194/acp-17-9599-2017.

——, H. Morrison, A. Varble, J. Berner, W. Wu, G. McFarquhar, and J. Milbrandt, 2019: Sensitivity of simulated deep convection to a stochastic ice microphysics framework. *J. Adv. Model. Earth Syst.*, **11**, 3362–3389, https://doi.org/10.1029/2019MS001730.

Strapp, J. W., L. E. Lilie, T. P. Ratvasky, C. R. Davison, and C. Dumont, 2016: Isokinetic TWC evaporator probe: Development of the IKP2 and performance testing for the HAIC-HIWC Darwin 2014 and Cayenne field campaigns. *Eighth AIAA Atmospheric and Space Environments Conf.*, Washington, DC, AIAA, 2016–4059, https://doi.org/10.2514/6.2016-4059.

Taszarek, M., J. T. Allen, T. Púčik, K. A. Hoogewind, and H. E. Brooks, 2020: Severe convective storms across Europe and the United States. Part II: ERA5 environments associated with lightning, large hail, severe wind, and tornadoes. *J. Climate*, **33**, 10 263–10 286, https://doi.org/10.1175/JCLI-D-20-0346.1.

Tobin, D. M., and M. R. Kumjian, 2021: Microphysical and polarimetric radar modeling of hydrometeor refreezing. *J. Atmos. Sci.*, **78**, 1965–1981, https://doi.org/10.1175/JAS-D-20-0314.1.

Um, J., and G. M. McFarquhar, 2011: Dependence of the single-scattering properties of small ice crystals on idealized shape models. *Atmos. Chem. Phys.*, **11**, 3159–3171, https://doi.org/10.5194/acp-11-3159-2011.

Van Weverberg, K., and Coauthors, 2013: The role of cloud microphysics parameterization in the simulation of mesoscale convective system clouds and precipitation in the tropical western Pacific. *J. Atmos. Sci.*, **70**, 1104–1128, https://doi.org/10.1175/JAS-D-12-0104.1.

Vázquez-Martín, S., T. Kuhn, and S. Eliasson, 2021a: Shape dependence of snow crystal fall speed. *Atmos. Chem. Phys.*, **21**, 7545–7565, https://doi.org/10.5194/acp-21-7545-2021.

——, ——, and ——, 2021b: Mass of different snow crystal shapes derived from fall speed measurements. *Atmos. Chem. Phys.*, **21**, 18 669–18 688, https://doi.org/10.5194/acp-21-18669-2021.

Wang, Y., H. Su, J. H. Jiang, F. Xu, and Y. L. Yung, 2020: Impact of cloud ice particle size uncertainty in a climate model and implications for future satellite missions. *J. Geophys. Res. Atmos.*, **125**, e2019JD032119, https://doi.org/10.1029/2019JD032119.

Wu, W., and G. M. McFarquhar, 2016: On the impacts of different definitions of maximum dimension for nonspherical particles recorded by 2D imaging probes. *J. Atmos. Oceanic Technol.*, **33**, 1057–1072, https://doi.org/10.1175/JTECH-D-15-0177.1.

Xue, L., and Coauthors, 2017: Idealized simulations of a squall line from the MC3E field campaign applying three bin microphysics schemes: Dynamic and thermodynamic structure. *Mon. Wea. Rev.*, **145**, 4789–4812, https://doi.org/10.1175/MWR-D-16-0385.1.